Modeling urban pollutant transport at multi-resolutions: Impacts of turbulent mixing

Zining Yang[1], Qiuyan Du[1], Qike Yang[1], Chun Zhao[1,2,3*], Gudongze Li[1], Zihan Xia[1],

Mingyue Xu[1], Renmin Yuan[1], Yubin Li[4], Kaihui Xia[1], Jun Gu[1], and Jiawang Feng[1]

[1]Deep Space Exploration Laboratory/School of Earth and Space Sciences/CMA-USTC Laboratory of Fengyun Remote Sensing/State Key Laboratory of Fire Science/Institute of Advanced Interdisciplinary Research on High-Performance Computing Systems and Software, University of Science and Technology of China, Hefei, China

[2]Laoshan Laboratory, Qingdao, China

[3]CAS Center for Excellence in Comparative Planetology, University of Science and Technology of China, Hefei, China.

[4]School of Atmospheric Physics, Nanjing University of Information Science and Technology, Nanjing, China

*Corresponding author: Chun Zhao (chunzhao@ustc.edu.cn)

Key Points:

1. Higher resolutions improve BC surface concentration predictions by enhancing PBL mixing and vertical wind flux, especially at night.

2. Small-scale eddies resolved at higher resolutions strengthen vertical fluxes, increasing BC atmospheric lifetime and column concentrations.

3. **Detailed land use and terrain in high-res models enhance PBL mixing, refining pollutant transport and urban air quality simulations.**

Abstract

Air pollution in cities seriously impacts public health and regional climate. Turbulent mixing plays a crucial role in pollutant formation and dissipation, yet current atmospheric models struggle to accurately represent it. The intensity of turbulent mixing varies with model resolution, which has rarely been analyzed. To investigate turbulent mixing variations at multi-resolutions and their implications for urban pollutant transport, we conducted numerical experiments using WRF-Chem at 25 km, 5 km, and 1 km resolutions. The simulated meteorological fields and black carbon (BC) concentrations are compared with observations. Differences in turbulent mixing across multi-resolutions are more pronounced at night, resulting in noticeable variations in BC concentrations. BC surface concentrations decrease as resolution increases from 25 km to 5 km and further to 1 km, but are similar at 5 km and 1 km resolutions. Enhanced planetary boundary layer (PBL) mixing coefficients and vertical wind flux at higher resolutions reduce the overestimation of nighttime BC surface concentrations. The 1 km resolution parameterized lower PBL mixing coefficients than 5 km but resolved more small-scale eddies, leading to similar near-surface turbulent mixing at both resolutions, while the intensity at higher altitudes is greater at 1 km. This caused BC to be transported higher and farther, increasing its atmospheric lifetime and column concentrations. Variations in mixing coefficients are partly attributed to differences in land use and terrain, with higher resolutions providing more detailed data that enhanced PBL mixing coefficients. This study interprets the impacts of turbulent mixing on simulated urban pollutant diffusion at multi-resolutions.

1. Introduction

Since the middle of the 19th century, rapid economic growth and urbanization have caused severe regional haze and photochemical smog pollution (Li et al., 2015; Li et al., 2019; Ma et al., 2019). A variety of air pollution episodes mainly occur in cities (Chan and Yao, 2008). Exposure to atmospheric particulate matter is one of the major threats to public health (Yin et al., 2017; Liu et al., 2019). Accurate pollutant estimation is crucial for the realization of pollution prevention goals. Pollution processes are affected by many different factors, such as pollution source emissions (Li et al., 2017a), physical and chemical characteristics of aerosols (Riccobono et al., 2014; Zhao et al., 2018), topographic effects (Zhang et al., 2018), and meteorological conditions (Ye et al., 2016). Significantly, pollutant concentrations are mainly gathered within the planetary boundary layer (PBL), and PBL mixing processes are associated with intricate turbulent eddies (Stull, 1988), which significantly affect the horizontal transport and vertical diffusion of pollutants (Wang et al., 2018; Du et al., 2020; Ren et al., 2020; Ren et al., 2021), as well as the formation of new aerosol particles (Wu et al., 2021).

The mechanism of turbulent transport has been widely investigated. The vertical diffusion of pollutants in urban areas is affected by the structure of the urban boundary layer (UBL), and different structures may lead to uneven spatial distribution of pollutants (Han et al., 2009; Zhao et al., 2013c). First, meteorological conditions play dominant roles in turbulent mixing of air pollutants within the atmospheric boundary layer (ABL) (Xu et al., 2015; Miao et al., 2019). Unstable meteorological conditions enhance turbulence, promoting pollutant dispersion, while stable conditions suppress it, leading to pollutants accumulation. Previous studies have indicated that constant stagnant winds and increased water vapor density inhibit the vertical diffusion of pollutants, resulting in explosive growth of pollutants (Zhang et al., 2015a; Zhang et al., 2015b; Wei et al., 2018; Zhong et al., 2018). Under these stable conditions, the inherent characteristics of the stable boundary layer (SBL), particularly turbulence intermittency (Costa et al., 2011), affect the heavy urban haze events by altering surface-atmosphere exchanges (Wei et al., 2018; Ren et al., 2019a; Ren et al., 2019b; Wei et al., 2020; Ren

85 et al., 2021; Zhang et al., 2022). Second, diurnal variations in turbulent mixing between

86 day and night significantly influence changes in pollutant concentrations (Li et al., 2018;

87 Liu et al., 2020). In the daytime convective boundary layer (CBL), pollutants can be

88 mixed uniformly in a thick layer due to the intense turbulent mixing (Sun et al., 2018).

89 While in the nighttime SBL, reduced mixing and dispersion result in the accumulation

90 of pollutants near the surface (Holmes et al., 2015). Severe urban haze pollution

91 formation is typically accompanied with the development of nocturnal SBL (Pierce et

92 al., 2019; Li et al., 2020; Zhang et al., 2020; Li et al., 2022). Moreover, pollutants in

93 the residual layer can be mixed downward to the surface with the development of the

94 ABL the next morning (Chen et al., 2009; Sun et al., 2013; Quan et al., 2020). Overall,

95 the impact of turbulent mixing on urban pollution is important and complex.

96   Numerical simulation is an important method for studying turbulent mixing.

97 However, there are still challenges associated with accurately representing turbulent

98 mixing in numerical models. Previous researches have indicated that turbulent mixing

99 in current atmospheric chemical models is insufficient to capture stable atmospheric

100 conditions, potentially leading to rapid increases in severe haze in urban areas (Ren et

101 al., 2019b; Wang et al., 2018; Peng et al., 2018; Du et al., 2020). Von Kuhlmann et al.

102 (2003) identified insufficient upward transport of ozone and its precursors due to weak

103 convection. Some studies revealed that WRF-Chem simulations underestimate

104 turbulent exchange within stable nocturnal boundary layers, allowing unrealistic

105 accumulation of pollutants near the surface (McKeen et al., 2007; Tuccella et al., 2012;

106 Berger et al., 2016). Additionally, PBL parameterization schemes in current models

107 may not accurately represent intricate turbulent mixing, particularly in complex terrains,

108 urban areas, or extreme weather conditions. Researches have revealed that different

109 PBL parameterization schemes employed in WRF-Chem tend to underestimate

110 turbulent mixing when compared to observations (Hong et al., 2006; Banks and

111 Baldasano, 2016; Kim, 2006). Turbulent mixing coefficients diagnosed in atmospheric

112 models characterize the intensity of turbulent mixing (Cuchiara et al., 2014). However,

113 these models frequently underestimate mixing coefficients during the nighttime.

114 Researchers have employed various approaches to address this limitation. Du et al.

115 (2020) demonstrated that increasing the lower limit of PBL mixing coefficients during

116 nighttime significantly reduced the modeling biases in simulated pollutant

117 concentrations. Jia and Zhang (2021) utilized the new modified turbulent diffusion

118 coefficient to represent the mixing process of pollutants separately and improved the

119 simulation results of pollutant concentrations. Jia et al. (2021) employed the revised

120 turbulent mixing coefficient of particles using high-resolution vertical flux data of

121 particles according to the mixing length theory, and improved the overestimation of

122 pollutant concentrations. In conclusion, current atmospheric models commonly face

123 several challenges in accurately simulating turbulent mixing.

124 The representation of turbulent mixing in models is influenced by various factors,

125 including grid resolution, topography, boundary layer parameterization, atmospheric

126 dynamics, and land-surface processes. Among these factors, model resolution can

127 significantly affect turbulent mixing processes in atmospheric simulations, with

128 simulated turbulent mixing varying substantially across different resolutions. Qian et al.

129 (2010) evaluated model performance at 3 km, 15 km, and 75 km resolutions, finding

130 that only simulations at 3 km resolution accurately captured multiple concentration

131 peaks in observational data, indicating that turbulent mixing may play a critical role in

132 simulating pollutant concentrations. Fountoukis et al. (2013) conducted model

133 simulations at three resolutions and demonstrated that higher resolution reduced the

134 bias for BC concentration by more than 30% in the Northeastern United States during

135 winter, attributing this improvement to better resolved pollutant dispersion. Tao et al.

136 (2020) found that changes in model resolution led to increased pollutant concentrations

137 in urban areas but decreased concentrations in west mountain regions, likely due to

138 differences in vertical and horizontal dispersion. In conclusion, previous researches

139 have primarily focused on comparing pollutant concentrations across different model

140 resolutions, demonstrating that resolution significantly affects pollutant distribution

141 and dispersion. These studies suggest that turbulent mixing may play a crucial role.

142 However, few have systematically explored the specific mechanisms by which

143 turbulent mixing influences pollutant concentrations simulated at multi-resolutions,

144 despite their importance in determining urban atmospheric pollutions.

145   Motivated by aforementioned problems, this study aims to investigate differences

146   in pollutant concentrations across multi-resolutions and explore how the turbulent

147   mixing plays as a crucial role affecting pollutant concentrations at various resolutions.

148   Furthermore, we seek to determine whether higher-resolution simulations can address

149   the issue of inaccurate turbulent mixing in current models. The Weather Research and

150   Forecasting model coupled with Chemistry (WRF-Chem) is applied to simulate

151   pollutant and meteorological fields during the spring of 2019 in Hefei, a typical mega-

152   city and sub-center of the Yangtze River Delta (YRD) urban agglomeration in China,

153   with a population of nearly 10 million and an area of 11,445 km^2. Our study interprets

154   the various characteristics of black carbon (BC) distributions simulated at multi-

155   resolutions and focuses on the mechanisms involved. BC is selected as the primary

156   pollutant for this study due to its near-inert nature in the atmosphere and can be treated

157   as a representative tracer for turbulent mixing. The paper is organized as follows:

158   Section 2 introduces the WRF-Chem model configuration, the design of multi-

159   resolutions experiments, emissions from different sources, and observational data.

160   Section 3 evaluates model simulations across multi-resolutions against observations,

161   presents the spatial distributions of surface and column concentrations simulated at

162   three resolutions, and investigates the important turbulent mixing processes that

163   generate spatial variability in pollutant concentrations. Section 4 present the conclusion

164   and discussion of the analysis.

165

2. Methodology

2.1 Models and Experiments

168   2.1.1 WRF-Chem

169   The non-hydrostatic Weather Research and Forecasting (WRF) model includes

170   various options for dynamic cores and physical parameterizations that can be used to

171   simulate atmospheric processes over a wide range of spatial and temporal scales

172   (Skamarock et al., 2008). WRF-Chem, the chemistry version of the WRF model (Grell

173   et al., 2005), simulates trace gases and particulates interactively with the meteorological

174 fields. WRF-Chem contains some treatments for photochemistry and aerosols

175 developed by the user community. In this study, the version of WRF-Chem updated by

176 the University of Science and Technology of China (USTC version of WRF-Chem) is

177 used. Compared with the publicly released version, this USTC version of WRF-Chem

178 includes some additional functions such as the diagnosis of radiative forcing of aerosol

179 species, land surface coupled biogenic VOC (volatile organic compound) emission,

180 aerosol-snow interaction, improved PBL mixing of aerosols and a detailed diagnosis of

181 the contributions of each crucial process to pollutant concentrations (Zhao et al., 2013a;

182 Zhao et al., 2013b; Zhao et al., 2014; Zhao et al., 2016; Hu et al., 2019; Du et al., 2020;

183 Zhang et al., 2021).

184   The configuration of WRF-Chem in this study is given in Table 1. The Statewide

185 Air Pollution Research Center (SAPRC99) photochemical mechanism (Carter, 2000) is

186 chosen to simulate the gas-phase chemistry, and the Model for Simulating Aerosol

187 Interactions and Chemistry (MOSAIC) is also selected (Zaveri and Peters, 1999; Zaveri

188 et al., 2008). The MOSAIC aerosol scheme includes important physical and chemical

189 processes such as nucleation, condensation, coagulation, aqueous-phase chemistry, and

190 water uptake by aerosols. Sulfate, nitrate, ammonium, sea salt, mineral dust, organic

191 matter (OM), BC, and other (unspecified) inorganics (OIN) constitute the prognostic

192 species in MOSAIC. The aerosol direct effect is coupled to the Rapid Radiative

193 Transfer Model (RRTMG) (Mlawer et al., 1997; Iacono et al., 2000) for both SW

194 (shortwave) and LW (longwave) radiation as implemented by Zhao et al. (2011). We

195 also turned on the aerosol indirect effect, which represents the interactions between

196 aerosols and clouds, including the first and second indirect effects,

197 activation/resuspension, wet scavenging, and aqueous chemistry (Gustafson et al., 2007;

198 Chapman et al., 2009). The photolysis rate is computed by the Fast-J radiation

199 parameterization (Wild et al., 2000). Our simulation includes the secondary organic

200 aerosol (SOA) mechanism, a crucial aerosol process that can substantially reduce

201 discrepancies between simulated results and observations.

202   Another type of option is meteorological physics, including the Yonsei University

203 (YSU) nonlocal PBL parameterization scheme (Hong et al., 2006), the Noah land-

204   surface model (Chen and Dudhia, 2001) for the surface layer process, the Morrison

205   two-moment scheme (Morrison et al., 2009) for cloud microphysics, and the Rapid

206   Radiative Transfer Model (RRTMG) for longwave and shortwave radiation. The 25 km

207   resolution simulation turns on the option of cumulus parameterization, which uses the

208   Kain-Fritsch cumulus and shallow convection scheme (Kain, 2004) to simulate sub-

209   grid scale clouds and precipitation. However, this option is turned off in the other two

210   higher resolution simulations because the fine-resolution is sufficient to resolve the

211   cloud forming processes.

212

213   2.1.2 Numerical experiments

214   The study period spans from March 5th to March 20th, 2019. Following previous

215   research (Gustafson et al., 2011), the first five days are considered as the model spin-

216   up time, while the remaining integration period is used for analysis. Consequently, only

217   the results from March 10th to March 20th, 2019, are used in the analysis of this study.

218   Three different resolutions and computational domains are employed in our study. The

219   outer domain, covering East, North, and South China, has 140 x 105 grid cells (107.1°-

220   127.9°E, 17.1°-44.9°N) with a horizontal resolution of 25 km. The middle domain,

221   encompassing the entire YRD region in East China, has 250 x 250 grid cells (111.82°-

222   121.78°E, 27.02°-36.98°N) with a resolution of 5 km. The inner domain, covering most

223   of the Hefei region, consists of 150 x 150 grid cells (116.604°-117.796°E, 31.204°-

224   32.396°N) at a horizontal resolution of 1 km. The center of inner domain is the city of

225   Hefei, a typical mega-city of East China. Hefei, the capital city of Anhui province, is

226   located in the mid-latitude zone with a humid subtropical monsoon climate and serves

227   as a representative case for this study. The regions are shown in Figure S1. To facilitate

228   the comparison of discrepancies among the three simulations at different resolutions,

229   we have selected the innermost region as the main scope of study for this research, as

230   shown in Figure 1a. In this study, we derive terrain information from a high-resolution

231   (~ 1 km) US Geological Survey (USGS) topographic data and interpolate it onto the

232   WRF grid. Therefore, the three domains with different resolutions exhibit varying

233   degrees of terrain detail. The 1 km grid resolves the most intricate topographic features,

234   followed by the 5 km grid, while the 25 km grid captures the least spatial detail. These

235   multi-resolutions topographic representations potentially influence pollutant turbulent

236   mixing processes, which will be analyzed in this study. The land cover dataset is derived

237   from a 1 km horizontal resolution dataset for China (Zhang et al., 2021). It provides a

238   more accurate representation of current land cover, particularly for eastern China,

239   which has experienced intensive urban expansion since the 2000s. Figure 1b shows the

240   land cover data at different resolutions, with detailed descriptions of the legend and

241   land cover classes provided in Table S1.

242   In order to allow for a straightforward comparison of multi-resolutions simulations

243   and facilitate the identification of differences between the high- and low-resolution

244   simulations, the corner locations of the 1 km and 5 km resolution domains are aligned

245   with the corner locations of the 25 km grid cell. Each grid cell in the 25 km simulation

246   consists of a 5 x 5 set of cells from the 5 km simulation, and each grid cell in the 5 km

247   simulation comprises 5 x 5 cells from the 1 km simulation, as shown in Figure S2. Thus,

248   exactly 25 grids at 5 km resolution and 625 grids at 1 km resolution are embedded

249   within each 25 km grid cell.

250   To ensure similar boundary forcing across the three simulations, initial and

251   boundary conditions are handled differently for the 25 km, 5 km, and 1 km resolution

252   domains. For the 25 km resolution, meteorological initial and lateral boundary

253   conditions are obtained from the National Center for Environmental Prediction (NCEP)

254   final reanalysis (FNL) data with 1° x 1° resolution and 6 h temporal resolution. Initial

255   and boundary conditions for the trace gases and aerosol species are provided by the

256   quasi-global WRF-Chem simulation with 360 x 145 grid cells (67.5°S-77.5°N, 180°W-

257   180°E) at 1° x 1° resolution. The initial and boundary conditions for the simulation at

258   5 km resolution are derived from the simulation at 25 km resolution. Similarly, the

259   initial and boundary conditions for the simulation at 1 km resolution are derived from

260   the simulation at 5 km resolution. In this way, since the forcing for the study area is

261   consistent across resolutions, differences in simulation results among multi-resolutions

262   can be attributed to disparities in model resolutions.

263

264   2.1.3 Emissions

265   Anthropogenic emissions for the outer quasi-global simulation are derived from the

266   Hemispheric Transport of Air Pollution version-2 (HTAPv2) at 0.1° x 0.1° horizontal

267   resolution and a monthly temporal resolution for 2010 (Janssens-Maenhout et al., 2015).

268   The Multi-resolution Emission Inventory for China (MEIC) at 0.25° x 0.25° horizontal

269   resolution for 2019 (Li et al., 2017a; Li et al., 2017b) is used to replace emissions over

270   China within the simulation domain. Emission differences significantly contribute to

271   pollutant concentration variability across multi-resolutions. Qian et al. (2010) showed

272   that sub-grid variability of emissions can contribute up to 50% of the variability near

273   Mexico City. To eliminate the impact of inconsistent emissions on pollutant

274   concentrations simulated at multi-resolutions, we ensured emission consistency

275   across the three domains by interpolating the 25 km resolution emissions of primary

276   species (NH_3, CO, NO_2, SO_2, BC, OC, $PM_{2.5}$, PM_{10}, SO_4, NO_3) to the 5 km and 1 km

277   resolution domains. This study primarily focuses on BC, the spatial distribution of BC

278   emissions is shown in Figure 2. Figure S3 illustrates BC emissions at three different

279   resolutions, demonstrating similar spatial patterns across multi-resolutions. Biomass

280   burning emissions are obtained from the Fire Inventory from NCAR (FINN) at 1 km

281   horizontal resolution and an hour temporal resolution (Wiedinmyer et al., 2011). The

282   diurnal variation of biomass burning emissions follows the suggestions by WRAP

283   (2005), with injection heights based on Dentener et al. (2006) from the Aerosol

284   Comparison between Observations and Models (AeroCom) project. Biogenic

285   emissions were calculated using the Model of Emissions of Gases and Aerosols from

286   Nature (MEGAN) v3.0 model (Zhang et al., 2021).

287

288   **2.2 Observational data**

289   2.2.1 Meteorological data

290   The meteorological data were obtained from the observation tower at the University

291   of Science and Technology of China (USTC) in Hefei, Anhui, China (117.27°E,

292   31.84°N), indicated by a solid black triangle in Figure 1a. The tower measures

293   temperature, relative humidity, wind speed, and wind direction at 2 m, 4.5 m, 8 m, 12.5

294 m and 18 m heights. This site represents a typical urban surface within the study area.

295 The tower was installed on the roof of a teaching building, with its top 17 m above the

296 canopy plane. It is equipped with three RM Young 03002 anemometers and three

297 HPM155A temperature and humidity sensors to measure the aforementioned

298 meteorological parameters (Yuan et al., 2016; Liu et al., 2017). This study focuses on

299 analyzing temperature, relative humidity, and wind speed.

300

301 2.2.2 BC surface concentration

302   In this study, we derived the hourly BC observations from the air quality monitoring

303 site on the campus of USTC during spring (March 10 to March 20, 2019). Hefei, a

304 major industrial and transportation hub, serves as the study area. In this study, we focus

305 on analyzing BC observational data to compare with model output. BC was observed

306 using a Multi-angle Absorption Photometer (MAAP, Model-5012) manufactured by

307 Thermo Scientific. This instrument is located approximately 260 m north of the USTC

308 meteorological tower. It takes advantage of the strong visible light absorption properties

309 of BC aerosols. There is a linear relationship between the attenuation of the beam after

310 passing through the aerosol sample and the load of BC aerosols on the fiber membrane.

311 The BC concentration is derived by inverting this relationship. A light scattering

312 measurement is incorporated into the chamber to correct for multiple scattering effects

313 caused by particle accumulation on the filter tape. The MAAP-5012 Black Carbon

314 Meter collects atmospheric aerosols using glass fiber filter membranes and observes

315 them at a wavelength of 670 nm.

316

317 **3. Results**

318 **3.1 Simulated meteorological fields at various resolutions**

319   Meteorological fields may play a crucial role in the turbulent mixing and pollutant

320 transport. Therefore, the time series of simulated temperature, wind speed, and relative

321 humidity are evaluated in this study. We evaluate simulated results at three resolutions

322 against observations to assess the impact of resolution on these key meteorological

323   variables. Figure 3a compares the time series of observed and simulated 8-m wind

324   speeds at the USTC site (117.27°E, 31.84°N). Simulation results among multi-

325   resolutions are similar, attributing to relatively flat and uncomplicated topography. The

326   temporal trends of the simulations closely align with observational data, exhibiting

327   distinct diurnal variations characterized by higher values during the daytime and lower

328   values at night. Additionally, the model struggles to capture some moments accurately,

329   overestimating wind speed when it suddenly increases. For instance, on March 20 at

330   noon, while the observed peak wind speed is approximately 6 m/s, simulations at 25

331   km and 5 km resolutions produced maximum wind speeds of approximately 9 m/s,

332   significantly exceeding the observed value, with only the 1 km resolution simulation

333   yielding results close to the observation. Figure 3b compares the 2-m temperature

334   simulated at three different resolutions with the observation. The multi-resolutions

335   simulation results exhibit remarkable consistency and closely align with observations.

336   Temperature displays a pronounced diurnal variation, fluctuating between 5 and 30 °C

337   with relative stability. However, the model occasionally underestimates or

338   overestimates values at certain time points. As shown in Figure 3c, the multi-resolutions

339   simulated results demonstrate consistency and accurately capture the diurnal variation

340   trend of observed relative humidity. Model results are highly consistent with

341   observations, both reaching a maximum of 100%. In summary, the simulated

342   meteorological variables across multi-resolutions demonstrate strong similarity and

343   closely match the observations, with only occasional minor discrepancies. However,

344   our subsequent analysis reveals that the variations in pollutant concentrations across

345   multi-resolutions cannot be attributed to the minor discrepancies observed in the time

346   series of meteorological variables.

347

348   **3.2 Simulated BC surface concentrations and impacts of turbulent mixing at**

349   **various resolutions**

350   3.2.1 Surface concentrations simulated at three different resolutions

351   The spatial distribution of BC surface concentrations across multi-resolutions in the

352   study area is illustrated in Figure 4. As the resolution improves from 25 km to 5 km and

353 further to 1 km, BC surface concentrations reveal more detailed spatial features. Figure

354 4a presents the simulation results across multi-resolutions, averaged over the whole day.

355 Significant variations exist from coarse resolutions to fine resolutions, with surface

356 concentrations decreasing as resolution increases from 25 km to 5 km and further to 1

357 km. BC surface concentrations range from 0 to 9 ug/m^3. At 25 km resolution, there is a

358 notable discrepancy between the spatial distributions of BC concentrations and

359 emissions (Fig. 2). The highest simulated concentration at 25 km resolution is located

360 west of the USTC site, while maximum emissions are centered at the USTC site. Our

361 analysis indicates that the difference in turbulent mixing between these two regions

362 leads to spatial inconsistency between BC surface concentrations and emissions. The

363 details of this phenomenon will be discussed in section 3.2.2. Figure 4b illustrates the

364 spatial distribution of BC surface concentrations during the daytime. The differences in

365 surface concentrations among multi-resolutions are minimal, with values falling within

366 the range of 0 to 5 ug/m^3. In the central urban areas, the BC surface concentration

367 simulated at 25 km resolution is marginally lower than those simulated at finer

368 resolutions. Moreover, during the daytime, simulated BC concentrations over Chaohu

369 lake areas are notably higher than in other regions, potentially due to the impact of dry

370 deposition velocity. Figure S4 shows the spatial distribution of dry deposition velocity,

371 revealing lower values over lakes compared to other areas. This lower dry deposition

372 velocity leads to higher pollutant concentrations over lakes compared to land areas after

373 pollutants transport to the lake surface during the daytime. At night, dry deposition

374 velocity is similar to that of surrounding non-urban land areas. Consequently, nighttime

375 BC concentrations over lakes are approximately equal to those in surrounding areas.

376 Figure 4c demonstrates the spatial distribution of BC surface concentrations during

377 nighttime. Compared to daytime, BC surface concentrations are notably higher in all

378 major urban regions at night, with high-resolution simulations capturing more spatial

379 variations. In conclusion, BC surface concentrations decrease as resolution increases

380 from 25 km to 5 km and further 1 km. However, the spatial distribution of BC surface

381 concentrations at 5 km and 1 km resolutions are similar throughout the whole day.

382   To facilitate a more accurate and direct comparison of results across multi-

383 resolutions, we refine coarse grids to match fine grids. The detailed refinement process

384 is described in Text S1. Figure S5a exhibits the spatial differences in BC surface

385 concentrations between 25 km and 5 km resolutions, as well as between 25 km and 1

386 km resolutions, averaged over the whole day. It reveals that coarse-resolution (25 km

387 resolution) simulations generally yield higher BC surface concentrations than fine-

388 resolutions (5 km and 1 km resolution) simulations across most areas. The largest

389 disparities mainly occur in central urban areas with complex underlying surfaces and

390 complicated flow patterns. Figure S5b demonstrate the spatial differences in BC surface

391 concentrations between 25 km and 5 km resolutions, as well as between 25 km and 1

392 km resolutions during the daytime, revealing smaller disparities mostly ranging

393 between -1 and 1 ug/m^3. In contrast, Figure S5c depicts pronounced differences in BC

394 concentrations between 25 km and 5 km resolutions, as well as between 25 km and 1

395 km resolutions during the nighttime, with most areas exhibiting disparities exceeding 2

396 ug/m^3. The largest differences are mainly concentrated in urban areas. These findings

397 indicate that diversities in BC surface concentrations among multi-resolutions are

398 primarily attributable to nocturnal concentrations in urban areas. However, differences

399 between 5 km and 1 km resolutions are small compared to those between 25 km and

400 finer resolutions (5 km and 1 km). BC surface concentrations are approximately equal

401 in the 5 km and 1 km simulations, as shown in Figure S6.

402   Furthermore, BC observations from the USTC monitoring station were utilized to

403 validate the simulated BC surface concentrations. Figure 5 illustrates the diurnal

404 variation of BC surface concentrations averaged over the Hefei region. Both

405 observations and simulations exhibit a pronounced diurnal variation, with lower

406 concentrations during the daytime and higher concentrations at night. During the

407 daytime, BC surface concentrations simulated at three resolutions are comparable to

408 the observational data. However, nighttime simulations significantly overestimate BC

409 surface concentrations. As resolution increases from 25 km to 5 km and 1 km, the

410 simulated surface concentrations decrease, aligning more closely with observations.

411 The 25 km resolution simulations yield the highest concentrations, with a maximum

412 value of approximately 12 ug/m^3, nearly double the observed values. In contrast, BC

413   surface concentrations simulated at 5 km and 1 km resolutions are similar and more

414   closely align with nocturnal observations, peaking at around 9 ug/m^3. In conclusion,

415   the diurnal variation of the observation is better captured by high-resolution (5 km and

416   1 km) simulations. The performance of BC surface concentrations across multi-

417   resolutions demonstrates that coarse grid spacing inadequately captures local pollutant

418   distributions. Previous studies have referred that the diurnal variation of BC surface

419   concentrations is mainly controlled by daily variations of PBL mixing and BC

420   emissions (Du et al., 2020). At night, pollutants are trapped within the shallow boundary

421   layer due to the reduced turbulent mixing, resulting in high BC surface concentrations.

422   As the boundary layer develops in the morning, pollutants rapidly diffuse and are

423   transported to upper layers, leading to relatively low surface concentrations. Therefore,

424   the turbulent mixing process plays a crucial role in determining pollutant concentrations.

425   To elucidate the mechanisms underlying the disparities in simulated BC surface

426   concentrations across multi-resolutions in urban areas, we conducted several in-depth

427   analyses to investigate the impact of turbulent mixing on pollutant concentrations.

428

429   3.2.2 Impacts of turbulent mixing on BC surface concentrations at three different

430   resolutions

431   To investigate the vertical mixing depth influencing pollutant diffusion, we first

432   analyze the PBL height, as illustrated in Figure 6. Figure 6a shows the spatial

433   distribution of the PBL height simulated at three different resolutions, averaged over

434   the whole day. Higher-resolution simulations yield lower PBL heights and capture more

435   intricate details compared to lower-resolution simulations. This trend is consistent

436   during both daytime and nighttime. Figure 6b demonstrates that the PBL height exceeds

437   0.9 km across most regions during the daytime. Notably, due to strong topographic

438   influences, the PBL height in the vicinity of Chaohu Lake is remarkably low, typically

439   less than 0.1 km. Conversely, in the southwestern region, characterized by higher

440   elevations and more complex terrain, the PBL height surpasses 1.1 km. Figure 6c

441   depicts the nighttime PBL heights at three different resolutions. These heights

442   predominantly fall below 0.3 km, significantly lower than those during the daytime.

443   The PBL height gradually decreases as the resolution increases, which should typically

444   lead to higher BC surface concentrations. However, BC surface concentrations actually

445   decrease as resolution increases from 25 km to 5 km and 1km (Figure 4). Consequently,

446   the PBL height alone cannot explain the differences in pollutant simulations among

447   multi-resolutions in this study.

448   Previous studies have established that PBL mixing coefficients are critical

449   determinants in air quality modeling (Du et al., 2020). In WRF-Chem, turbulent mixing

450   within the boundary layer is partially governed by PBL mixing coefficients simulated

451   by the PBL parameterization scheme. The spatial distribution of turbulent mixing

452   coefficients at the lowest model layer is analyzed, as shown in Figure 7. Figure 7a

453   illustrates the simulation results across multi-resolutions averaged over the whole day.

454   The variations in PBL mixing coefficients across different resolutions are evident, with

455   high-resolution simulations capturing more spatial characteristics. The spatial

456   distribution of the PBL mixing coefficient demonstrates strong correlation with land

457   use type and terrain height, which will be explored subsequently. Turbulent mixing

458   coefficients range from 0 to 8 m^2/s, with peak values predominantly located in urban

459   areas. Notably, the mixing coefficient simulated at 25 km resolution near surface around

460   USTC substantially exceeds that of the western area, resulting in lower BC surface

461   concentrations simulated at 25 km resolution at USTC compared to its western regions

462   (Figure 4). This discrepancy leads to a mismatch between the spatial distribution of

463   pollutant concentrations and emissions, as discussed in section 3.2.1. During the

464   daytime, the PBL mixing coefficients simulated at three resolutions are relatively high,

465   ranging from 0 to 17 m^2/s, as shown in Figure 7b. BC masses simulated across multi-

466   resolutions are fully mixed within the boundary layer, resulting in similar BC surface

467   concentrations across these resolutions. Conversely, turbulent mixing coefficients

468   diminish considerably during the nighttime, with maximum values approximately 3

469   m^2/s, as shown in Figure 7c. The turbulent mixing coefficient emerges as one of the

470   important factors controlling surface pollutant concentrations under stable nocturnal

471   PBL conditions. Nighttime PBL coefficients are higher at 5 km and 1 km resolutions

472   compared to 25 km resolution across most of the study area, resulting in lower BC

473 surface concentrations at these two higher resolutions during the nighttime. Figure S7

474 further illustrates the disparities in parametrized PBL mixing coefficients between 25

475 km resolution and the two higher-resolution simulations. However, in the lowest model

476 layer, Figure S8 shows that the intension of turbulent mixing parameterized at 5 km

477 resolution is larger than that at 1 km resolution, which fails to explain the similar surface

478 concentrations in these two higher-resolution (5 km and 1 km) simulations. To further

479 investigate this phenomenon, we selected a meridional section passing through the

480 USTC site to analyze the distribution of vertical wind speed flux, which represents the

481 turbulent mixing directly resolved by large-scale dynamic processes.

482  Figure 8 displays the cross section of meridional wind speed flux along the USTC

483 site simulated at three different resolutions. The upward vertical wind speed flux

484 simulated at 25 km resolution are near the surface. However, the 5 km resolution

485 simulation generates stronger upward motion at a slightly higher altitude, specifically

486 between 850 and 1000 hPa. Notably, the 1 km resolution simulation captures the highest

487 vertical wind speed flux, with relatively intensive upward motion extending beyond

488 500 hPa. The 1 km resolution can resolve small-scale eddies and capture the most

489 pronounced vertical wind speed fluxes. In comparison, simulations at 5 km resolution

490 are able to capture smaller-scale eddies, while those at 25 km resolution occasionally

491 capture larger-scale eddies. Despite the larger PBL mixing coefficients at 5 km

492 resolution compared to 1 km resolution near the surface, the upward vertical wind speed

493 flux at 1 km resolution reaches higher altitudes, indicating the presence of more small-

494 scale eddies and resulting in enhanced vertical turbulent mixing. Consequently, near the

495 surface, the combined effects of turbulent mixing, which is represented by both the

496 parameterized PBL mixing coefficient and the directly resolved vertical wind speed

497 flux, lead to similar BC surface concentrations at higher resolutions (5 km and 1 km)

498 simulations. Furthermore, Figure S9 shows the meridional cross section during daytime

499 and nighttime. During the day, the mixing height vertically upward is relatively high at

500 all three resolutions, allowing pollutants to be fully mixed and transported within the

501 PBL. This results in similar BC surface concentrations across multi-resolutions.

502 Conversely, at night, high-resolution simulations resolve more small-scale eddies,

503   resulting in vertical transport reaching higher altitudes and intensifying turbulent

504   mixing. In conclusion, pollutants in lower-resolutions (25 km) simulations tend to

505   accumulate near the surface, whereas at higher resolutions (5 km and 1 km) simulations,

506   pollutants are transported to higher heights. This phenomenon contributes to imparities

507   in BC surface concentration across multi-resolutions.

508   Previous analysis indicate that the PBL mixing coefficient is one of the main factors

509   contributing to the disparities in BC surface concentrations across multi-resolutions.

510   Therefore, we further explored the factors influencing the spatial distribution of the

511   PBL mixing coefficient. Our analysis reveals that the spatial distribution of the PBL

512   mixing coefficient is closely related to land use types and terrain height. Specifically,

513   the overall distribution of the turbulent mixing coefficient is closely resembled by the

514   land use types (Figure 1b and Figure 7). However, in areas with obvious magnitude

515   changes, such as east of the USTC site, the turbulent mixing coefficient displays distinct

516   gradient changes that are not reflected in land use patterns. Notably, the spatial

517   distribution of the topographic height (Figure 1a) in this region exhibits distinct gradient

518   changes similar to those of the turbulent mixing coefficients. Consequently, the spatial

519   distribution of the turbulent mixing coefficient is influenced by both terrain and land

520   use types. This correlation can be attributed to the inter-relationship among turbulent

521   mixing, friction velocity, terrain, and land use types. Terrain and land use types

522   influence friction velocity by modifying surface roughness, which in turn directly

523   affects turbulent mixing coefficients within the PBL. Higher surface roughness

524   typically lead to greater fiction velocity, subsequently enhancing turbulent intensity and

525   increasing the vertical mixing efficiency of pollutants within the PBL. To further

526   investigate this relationship, the spatial distribution of friction velocity is analyzed, as

527   shown in Figure 9. The analysis reveals that friction velocity increases as resolution

528   increases from 25 km to 5 km and 1 km resolutions, with finer resolutions (5 km and 1

529   km) capturing more spatial details. Differences in friction velocity are illustrated in

530   Figure S10. The spatial distribution of friction velocity indeed correlates with terrain

531   and land use patterns, consequently influencing the distribution of the PBL mixing

532   coefficient. As a result, the spatial distribution of the PBL mixing coefficient correlates

533   with land use types and terrain height.

534   Our study indicates that variations in land use type distribution simulated at

535   different resolutions are a significant factor causing changes in PBL mixing coefficient

536   across multi-resolutions. These variations in mixing coefficients relate closely to BC

537   surface concentrations, explaining specific patterns of BC surface concentration

538   distributions. For example, the BC surface concentration south of the USTC site

539   increases as resolution improves from 25 km to 5 km and 1 km resolutions (Figure 4

540   and Figure S5), contrasting with concentration variations simulated in other regions.

541   Our analysis reveals that the turbulent mixing coefficient simulated at 25 km resolution

542   is higher compared to the two higher-resolution simulations in this area (Figure 7 and

543   Figure S7). Moreover, the spatial distribution of land use types indicates that the 25 km

544   resolution simulation resolves only a single urban land use type in this area (Figure 1b).

545   In contrast, higher resolution simulations capture additional land use types beyond the

546   urban, including lakes, farmland, and shrubs (Figure 1b). The inclusion of these diverse

547   land use types in the higher resolution leads to smaller PBL mixing coefficients in this

548   area, as the surface roughness associated with lakes, farmland, and shrubs is generally

549   lower than that of urban areas. As a result, the reduced vertical mixing in the finer

550   resolution (5 km and 1 km) simulations results in higher BC surface concentrations

551   south of the USTC site.

552

553   **3.3 Simulated BC column concentrations and impacts of turbulent mixing at**

554   **various resolutions**

555   3.3.1 Simulated BC column concentrations at three different resolutions

556   It is generally accepted that the turbulent mixing process primarily affects

557   pollutant surface concentrations by mixing surface pollutants into higher layers,

558   without altering the column concentration. However, in this study, BC column

559   concentrations exhibit differences across multi-resolutions simulations. Therefore, we

560   further investigate the spatial distribution of BC column concentrations and the main

561   mechanisms behind these variations. Figure 10a illustrates the spatial distribution of

562   BC column concentrations simulated at three resolutions, averaged over the whole day.

563   The regional average values for the three resolutions are 2041, 2150, and 2223 ug/m^2,

564   respectively. The 5 km and 1 km resolution simulations yield larger BC column

565   concentrations compared to 25 km resolution simulations. The spatial distribution of

566   BC column concentrations simulated at 25 km resolution is highly consistent with the

567   BC emission distributions (Figure 2), showing high concentrations in central urban

568   areas exceeding 2500 ug/m^2, while regions distant from urban centers demonstrate

569   lower concentrations, generally below 2100 ug/m^2. The 5 km resolution simulation

570   results indicate peak column concentrations concentrated in urban areas and spread

571   around, with the southwestern area approaching 2250 ug/m^2. The 1 km resolution

572   simulation results yield the largest BC column concentrations and demonstrate the most

573   pronounced diffusion tendency, with most areas exceeding 2250 ug/m^2. Figure 10b and

574   Figure 10c reveal lower BC column concentrations during the daytime compared to

575   those at night, with a more pronounced dispersion trend of column concentrations

576   simulated at night. Figure S11 depicts the differences in BC column concentrations

577   between 25 km and 5 km resolutions, as well as between 25 km and 1 km resolutions,

578   revealing that BC column concentrations in coarser resolutions are marginally lower

579   than those in finer resolutions (5 km and 1 km) in most of the study areas. On the other

580   hand, the BC column concentration simulated at 1 km resolution are larger than those

581   at 5 km resolution, as shown in Figure S12. In conclusion, BC column concentrations

582   increases with increased resolutions, accompanied by a more pronounced dispersion

583   tendency towards higher and farther areas.

584

585   3.3.2 Impacts of turbulent mixing on BC column concentrations at three different

586   resolutions

587   We further analyze the mechanisms underlying the differences in BC column

588   concentrations across multi-resolutions in urban areas. Figure 11a displays the vertical

589   profiles of BC concentrations averaged over the study area. The BC profiles at 25 km

590   resolution exhibit significant variability, generally decreasing from the surface to higher

591   altitudes. The near-surface BC concentration is approximately three times higher than

592   those at high altitudes, with surface concentrations reaching about 3 ug/m^3. At an

593   altitude of 100 m, the concentration drops to 1 ug/m^3, while above this elevation, the

594   BC concentration is less than 1 ug/m^3. Substantial disparities exist among multi-

595   resolutions simulations in the vertical profiles of BC concentrations. Our analyses

596   above have shown that near the surface, the parameterized mixing coefficients and

597   directly resolved vertical wind speed flux are lower at 25 km resolution compared to 5

598   km and 1 km resolutions, reducing the vertical mixing of pollutants in 25 km resolution

599   simulations. Thus, BC concentrations at 25 km resolution are higher near the surface

600   and lower at higher altitudes compared to high-resolution (5 km and 1 km) simulations.

601   Moreover, the parametrized PBL mixing coefficient at 1 km resolution is lower than at

602   5 km resolution in the atmosphere, but the directly resolved upward vertical wind speed

603   flux by the model dynamic process reaches higher altitudes at 1 km resolution compared

604   to 5 km resolution. Thus, due to the combined effects of these two processes, the

605   intensity of turbulent mixing is similar between the 5 km and 1 km resolutions at near-

606   surface levels, whereas it is greater at 1 km resolution than at 5 km resolution at higher

607   altitudes. In numerical models, sub-grid scale (SGS) turbulent diffusion is typically

608   simulated by parameterization schemes. However, as model resolution increases, such

609   as achieving 1 km resolution, the turbulent mixing is increasingly resolved by the

610   dynamical framework of model. This advancement allows the model to capture

611   dynamic structures and small-scale turbulence more accurately, significantly enhancing

612   the strength of turbulent mixing. The direct resolve of dynamic processes reduces

613   reliance on traditional parameterization schemes, thereby decreasing the PBL mixing

614   coefficient parameterized at finer resolutions. In conclusion, at higher altitudes, the

615   enhanced turbulent mixing efficiently facilitates more ground-emitted pollutants to

616   higher height as resolution increases. Thus, BC concentrations at 5 km and 1 km

617   resolution are similar near surface, with 1 km resolution yielding the largest

618   concentrations at higher altitudes.

619   To further investigate the BC column concentrations and their dispersion tendency

620   towards farther areas, we analyzed the vertical profile of wind speed at three resolutions

621   averaged over the study area, as shown in Figure 11b. The vertical profile of wind speed

622   is relatively consistent across the three resolutions. From the ground to higher altitudes,

the overall wind speed gradually increases, transitioning from low speeds near the surface to higher speeds aloft. Near the ground, the simulated average wind speed is approximately 1 m/s, increasing to 4 m/s at an altitude of 1 km, and reaching an average of about 7 m/s at an altitude of 2 km. In the upper atmosphere, characterized by larger wind speeds, pollutants mixed up from near-surface can be transported and dispersed farther. As previously mentioned, BC simulated in higher-resolution simulations can be transported to higher altitudes, thus dispersing over greater distances by stronger winds. Therefore, as the resolution increases, the trend of diffusion towards farther regions in the simulated BC column concentrations becomes more pronounced.

As previously discussed, higher-resolution simulations facilitate BC transport to greater altitudes and further distances. This phenomenon extends its atmospheric lifetime, consequently resulting in increased column concentrations. Bauer et al. (2013) noted that turbulent mixing and convective transport processes play a critical role in determining BC lifetimes. Figure 12 illustrates the spatial distribution of BC lifetime, calculated by dividing the BC column concentration by the dry deposition flux. It demonstrates that BC lifetime gradually lengthens as resolution increases. The average lifetime of BC column concentrations in the study area is 344 h, 350 h, and 382 h for 25 km, 5 km, and 1 km resolutions, respectively. These results clearly demonstrate that BC simulated at higher resolutions exhibits prolonged atmospheric residence times. Consequently, the BC column concentration is higher in high-resolution simulations.

4. Conclusion and Discussion

Turbulent mixing plays a crucial role in urban pollutant transport by enhancing the diffusion of atmospheric pollutants. Current atmospheric models often underestimate turbulent exchange within stable nocturnal boundary layers, and the turbulent mixing varies markedly across different model resolutions. However, few studies have analyzed how turbulent mixing processes across multi-resolutions affect pollutant concentrations in urban areas. Therefore, our goal is to elucidate the variations in pollutant concentrations across multi-resolutions and investigate the influence of

652   turbulent mixing on pollutant concentrations at various resolutions.

653   We conducted a three-nested WRF-Chem simulation at 25 km, 5 km, and 1 km

654   resolutions in the Hefei area. BC surface concentrations decrease as resolution increases

655   from 25 km to 5 km and further to 1 km but are similar at 5 km and 1 km resolutions,

656   showing significant diurnal variations with higher concentrations at night and lower

657   during the daytime. The BC surface concentrations across multi-resolutions align well

658   with USTC site observations during daytime but are overestimated at night, with this

659   overestimation decreasing at higher-resolution (5 km and 1 km). Disparities in BC

660   surface concentrations between the two finer-resolution and the 25 km resolution

661   simulations are primarily attributable to nocturnal concentrations. The PBL mixing

662   coefficient plays a crucial role in controlling surface pollutant concentrations at night.

663   Larger nighttime PBL mixing coefficients and higher vertical wind speed flux at 5 km

664   and 1 km resolutions compared to 25 km resolution near the surface result in lower BC

665   surface concentrations. However, the PBL mixing coefficient at 5 km is larger than at

666   1 km resolution. Moreover, the upward vertical wind speed flux resolved at 1 km

667   resolution reaches higher altitudes compared to 25 km and 5 km resolutions, indicating

668   more small-scale eddies and resulting in enhanced turbulent mixing. Consequently, near

669   the surface, the combined effects of parametrized PBL mixing coefficient and the

670   directly resolved vertical wind speed flux lead to similar BC surface concentrations at

671   5 km and 1 km resolutions.

672   Further analysis reveals that the spatial distribution of PBL mixing coefficients is

673   influenced by both land use types and terrain heights. The turbulent mixing coefficient

674   correlates with the spatial distribution of land use types at smaller scales, while

675   correlating with terrain heights at larger scales, particularly in regions with complex

676   topography and complicated flow patterns. This correlation can be attributed to the

677   interrelationship among turbulent mixing coefficients, friction velocity, terrain, and

678   land use types. The static database of terrain and land use types employed as model

679   input determines the surface roughness. Higher surface roughness typically leads to

680   greater fiction velocity, subsequently increasing the PBL mixing coefficients.

681   The variations in turbulent mixing across multi-resolution simulations not only

682 affect the BC surface concentration but also lead to different BC column concentrations.

683 BC column concentrations increase with improved resolutions, accompanied by a more

684 pronounced diffusion tendency towards higher altitudes and distant regions.

685 Throughout the atmosphere, turbulent mixing intensifies with improved resolutions,

686 resulting in pollutants being transported to higher altitudes. Concurrently, wind speed

687 increases with altitude, facilitating the pollutants which are mixed to higher altitudes to

688 be spread farther. Consequently, BC simulated at higher resolution is transported to

689 greater altitudes and dispersed to farther regions, thus persisting in the atmosphere for

690 longer periods and leading to larger lifetimes. As a result, BC column concentrations

691 increase with finer resolutions.

692 This study highlights the importance of model resolution in simulating the

693 dispersion of atmospheric pollutants. We observed that the enhanced turbulent mixing

694 strength in high-resolution can more accurately reproduce the vertical and horizontal

695 distribution of pollutants, thus aligning the simulated pollutant surface concentrations

696 more closely with actual observations. In contrast, turbulent mixing in low-resolution

697 simulations, primarily depending on boundary layer parameterizations, may not

698 adequately capture the dynamics of turbulence, leading to discrepancies between the

699 simulated and actual distribution of pollutants, particularly during the night with stable

700 boundary condition. Future research should focus on improving PBL parameterization

701 schemes to enhance model performance at lower resolutions, thereby better serving the

702 needs of air pollution control and environmental management.

703 Moreover, we have noted that the parameterized PBL mixing coefficient decreases

704 when transitioning from 5 km to 1 km resolution, alongside an increase in vertical wind

705 speed flux which represents turbulent mixing directly resolved by the dynamical

706 processes. This trend suggests that if the resolution was further increased to LES scales,

707 the parameterized PBL mixing coefficient might diminish significantly, potentially

708 approaching zero, while the turbulence mixing resolved directly by the dynamics would

709 intensify considerably. At LES scales, the majority of turbulent mixing is directly

710 resolved, capturing the atmospheric dynamical processes and turbulent exchanges more

711 realistically, thereby reducing the simulation biases caused by parameterization errors.

712   This shift diminishes reliance on traditional boundary layer parameterizations to
713   simulate turbulent mixing, leading to a substantial reduction in the parameterized
714   boundary layer mixing coefficient. By capturing the finer details of atmospheric
715   dynamics, the model provides a more realistic representation of turbulent mixing and
716   related physical processes, which is crucial for understanding weather patterns, climate
717   variability, and pollutant dispersion. However, due to the huge computational resources
718   required for LES simulation, we have not yet performed an analysis at the LES scale,
719   but it is worth further exploring in the future.

720   Our analysis also found that higher-resolution facilitate transport over greater
721   distances, suggesting that inter-city pollutant diffusion can be affected by model
722   resolution, with coarse-resolution potentially reducing long-range transport and inter-
723   urban impacts. While previous studies have examined pollutant formation mechanisms
724   at specific resolutions and explored the physical and chemical interactions among
725   megacities, few have considered the impacts of different resolutions on long-range
726   transport between cities. Due to computational cost constraints, inter-urban impacts are
727   not discussed in this study but deserve further investigation in the future. Furthermore,
728   this study focuses exclusively on BC, a primary aerosol species, while the impact of
729   grid resolution on secondary aerosols may differ. Future investigations could expand
730   this analysis to encompass a wider spectrum of pollutant species.

731

732

733

734

735

736

737

738

739

740

741

Data availability. The release version of WRF-Chem can be downloaded from http://www2.mmm.ucar.edu/wrf/users/download/get_source.html. The updated USTC version of WRF-Chem can be downloaded from http://aemol.ustc.edu.cn/product/list/ or contact chunzhao@ustc.edu.cn. Additionally, code modifications will be incorporated into the release version of WRF-Chem in the future.

Author contributions. Zining Yang and Chun Zhao designed the experiments and conducted and analyzed the simulations. All authors contributed to the discussion and final version of the paper.

Competing interests. The contact author has declared that none of the authors has any competing interests.

Acknowledgments. This research was supported by the National Key Research and Development Program of China (No. 2022YFC3700701), the Strategic Priority Research Program of Chinese Academy of Sciences (XDB0500303), National Natural Science Foundation of China (41775146), the USTC Research Funds of the Double First-Class Initiative (YD2080002007, KY2080000114), the Science and Technology Innovation Project of Laoshan Laboratory (LSKJ202300305), and the National Key Scientific and Technological Infrastructure project "Earth System Numerical Simulation Facility" (EarthLab). The study used the computing resources from the Supercomputing Center of the University of Science and Technology of China (USTC) and the Qingdao Supercomputing and Big Data Center.

Reference

Banks, R. F. and Baldasano, J. M.: Impact of WRF model PBL schemes on air quality simulations over Catalonia, Spain, Science of the Total Environment, 572, 98-113, https://doi.org/10.1016/j.scitotenv.2016.07.167, 2016.

Bauer, S. E., Bausch, A., Nazarenko, L., Tsigaridis, K., Xu, B., Edwards, R., Bisiaux, M., and McConnell, J.: Historical and future black carbon deposition on the three ice caps: Ice core measurements and model simulations from 1850 to 2100, Journal of Geophysical Research-Atmospheres, 118, 7948-7961, https://doi.org/10.1002/jgrd.50612, 2013.

Berger, A., Barbet, C., Leriche, M., Deguillaume, L., Mari, C., Chaumerliac, N., Begue, N., Tulet, P., Gazen, D., and Escobar, J.: Evaluation of Meso-NH and WRF-CHEM simulated gas and aerosol chemistry over Europe based on hourly observations, Atmospheric Research, 176, 43-63, https://doi.org/10.1016/j.atmosres.2016.02.006, 2016.

Carter: Implementation of the SAPRC-99 chemical mechanism into the models-3 framework, 2000.

Chan, C. K. and Yao, X.: Air pollution in mega cities in China, Atmospheric Environment, 42, 1-42, https://doi.org/10.1016/j.atmosenv.2007.09.003, 2008.

Chapman, E. G., Gustafson, W. I., Jr., Easter, R. C., Barnard, J. C., Ghan, S. J., Pekour, M. S., and Fast, J. D.: Coupling aerosol-cloud-radiative processes in the WRF-Chem model: Investigating the radiative impact of elevated point sources, Atmospheric Chemistry and Physics, 9, 945-964, https://doi.org/10.5194/acp-9-945-2009, 2009.

Chen, F. and Dudhia, J.: Coupling an Advanced Land Surface–Hydrology Model with the Penn State–NCAR MM5 Modeling System. Part I: Model Implementation and Sensitivity, Monthly Weather Review, 129, 569-585, 2001.

Chen, Y., Zhao, C., Zhang, Q., Deng, Z., Huang, M., and Ma, X.: Aircraft study of Mountain Chimney Effect of Beijing, China, Journal of Geophysical Research-Atmospheres, 114, https://doi.org/10.1029/2008jd010610, 2009.

793   Costa, F. D., Acevedo, O. C., Mombach, J. C. M., and Degrazia, G. A.: A Simplified

794   Model for Intermittent Turbulence in the Nocturnal Boundary Layer, Journal of the

795   Atmospheric Sciences, 68, 1714-1729, https://doi.org/10.1175/2011jas3655.1,

796   2011.

797   Cuchiara, G. C., Li, X., Carvalho, J., and Rappenglueck, B.: Intercomparison of

798   planetary boundary layer parameterization and its impacts on surface ozone

799   concentration in the WRF-Chem model for a case study in Houston/Texas,

800   Atmospheric Environment, 96, 175-185,

801   https://doi.org/10.1016/j.atmosenv.2014.07.013, 2014.

802   Dentener, F., Kinne, S., Bond, T., Boucher, O., Cofala, J., Generoso, S., Ginoux, P.,

803   Gong, S., Hoelzemann, J. J., Ito, A., Marelli, L., Penner, J. E., Putaud, J. P., Textor,

804   C., Schulz, M., van der Werf, G. R., and Wilson, J.: Emissions of primary aerosol

805   and precursor gases in the years 2000 and 1750 prescribed data-sets for AeroCom,

806   Atmospheric Chemistry and Physics, 6, 4321-4344, https://doi.org/10.5194/acp-6-

807   4321-2006, 2006.

808   Du, Q., Zhao, C., Zhang, M., Dong, X., Chen, Y., Liu, Z., Hu, Z., Zhang, Q., Li, Y.,

809   Yuan, R., and Miao, S.: Modeling diurnal variation of surface $PM_{2.5}$ concentrations

810   over East China with WRF-Chem: impacts from boundary-layer mixing and

811   anthropogenic emission, Atmospheric Chemistry and Physics, 20, 2839-2863,

812   https://doi.org/10.5194/acp-20-2839-2020, 2020.

813   Fountoukis, C., Koraj, D., van der Gon, H. A. C. D., Charalampidis, P. E., Pilinis, C.,

814   and Pandis, S. N.: Impact of grid resolution on the predicted fine PM by a regional

815   3-D chemical transport model, Atmospheric Environment, 68, 24-32,

816   https://doi.org/10.1016/j.atmosenv.2012.11.008, 2013.

817   Grell, G. A., Peckham, S. E., Schmitz, R., McKeen, S. A., Frost, G., Skamarock, W. C.,

818   and Eder, B.: Fully coupled "online" chemistry within the WRF model,

819   Atmospheric Environment, 39, 6957-6975,

820   https://doi.org/10.1016/j.atmosenv.2005.04.027, 2005.

821   Gustafson, W. I., Jr., Qian, Y., and Fast, J. D.: Downscaling aerosols and the impact of

822   neglected subgrid processes on direct aerosol radiative forcing for a representative

823   global climate model grid spacing, Journal of Geophysical Research-Atmospheres,

824   116, https://doi.org/10.1029/2010jd015480, 2011.

825   Gustafson, W. I., Jr., Chapman, E. G., Ghan, S. J., Easter, R. C., and Fast, J. D.: Impact

826   on modeled cloud characteristics due to simplified treatment of uniform cloud

827   condensation nuclei during NEAQS 2004, Geophysical Research Letters, 34,

828   https://doi.org/10.1029/2007gl030021, 2007.

829   Han, S., Bian, H., Tie, X., Xie, Y., Sun, M., and Liu, A.: Impact of nocturnal planetary

830   boundary layer on urban air pollutants: Measurements from a 250-m tower over

831   Tianjin, China, Journal of Hazardous Materials, 162, 264-269,

832   https://doi.org/10.1016/j.jhazmat.2008.05.056, 2009.

833   Holmes, H. A., Sriramasamudram, J. K., Pardyjak, E. R., and Whiteman, C. D.:

834   Turbulent Fluxes and Pollutant Mixing during Wintertime Air Pollution Episodes

835   in Complex Terrain, Environmental Science & Technology, 49, 13206-13214,

836   https://doi.org/10.1021/acs.est.5b02616, 2015.

837   Hong, S.-Y., Noh, Y., and Dudhia, J.: A new vertical diffusion package with an explicit

838   treatment of entrainment processes, Monthly Weather Review, 134, 2318-2341,

839   https://doi.org/10.1175/mwr3199.1, 2006.

840   Hu, Z., Huang, J., Zhao, C., Bi, J., Jin, Q., Qian, Y., Leung, L. R., Feng, T., Chen, S.,

841   and Ma, J.: Modeling the contributions of Northern Hemisphere dust sources to

842   dust outflow from East Asia, Atmospheric Environment, 202, 234-243,

843   https://doi.org/10.1016/j.atmosenv.2019.01.022, 2019.

844   Iacono, M. J., Mlawer, E. J., Clough, S. A., and Morcrette, J. J.: Impact of an improved

845   longwave radiation model, RRTM, on the energy budget and thermodynamic

846   properties of the NCAR community climate model, CCM3, Journal of Geophysical

847   Research-Atmospheres, 105, 14873-14890, https://doi.org/10.1029/2000jd900091,

848   2000.

849   Janssens-Maenhout, G., Crippa, M., Guizzardi, D., Dentener, F., Muntean, M., Pouliot,

850   G., Keating, T., Zhang, Q., Kurokawa, J., Wankmueller, R., van der Gon, H. D.,

851   Kuenen, J. J. P., Klimont, Z., Frost, G., Darras, S., Koffi, B., and Li, M.:

852   HTAP_v2.2: a mosaic of regional and global emission grid maps for 2008 and 2010

853   to study hemispheric transport of air pollution, Atmospheric Chemistry and

854   Physics, 15, 11411-11432, https://doi.org/10.5194/acp-15-11411-2015, 2015.

855   Jia, W. and Zhang, X.: Impact of modified turbulent diffusion of $PM_{2.5}$ aerosol in WRF-

856   Chem simulations in eastern China, Atmospheric Chemistry and Physics, 21,

857   16827-16841, https://doi.org/10.5194/acp-21-16827-2021, 2021.

858   Jia, W., Zhang, X., Zhang, H., and Ren, Y.: Application of Turbulent Diffusion Term of

859   Aerosols in Mesoscale Model, Geophysical Research Letters, 48,

860   https://doi.org/10.1029/2021gl093199, 2021.

861   Kain, J. S.: The Kain-Fritsch convective parameterization: An update, Journal of

862   Applied Meteorology, 43, 170-181, https://doi.org/10.1175/1520-

863   0450(2004)043<0170:Tkcpau>2.0.Co;2, 2004.

864   Kim, S. W.: The Influence of PBL Parameterizations on the Distributions of Chemical

865   Species in a Mesoscale Chemical Transport Model, WRF-Chem,

866   Li, H., Li, L., Huang, C., An, J., Yan, R., Huang, H., Wang, Y., Lu, Q., Wang, Q., Lou,

867   S., Wang, H., Zhou, M., Tao, S., Qiao, L., and Chen, M.: Ozone Source

868   Apportionment at Urban Area during a Typical Photochemical Pollution Episode

869   in the Summer of 2013 in the Yangtze River Delta, Environmental Science, 36, 1-

870   10, 2015.

871   Li, L., An, J., Huang, L., Yan, R., Huang, C., and Yarwood, G.: Ozone source

872   apportionment over the Yangtze River Delta region, China: Investigation of

873   regional transport, sectoral contributions and seasonal differences, Atmospheric

874   Environment, 202, 269-280, https://doi.org/10.1016/j.atmosenv.2019.01.028,

875   2019.

876   Li, M., Liu, H., Geng, G., Hong, C., Liu, F., Song, Y., Tong, D., Zheng, B., Cui, H.,

877   Man, H., Zhang, Q., and He, K.: Anthropogenic emission inventories in China: a

878   review, National Science Review, 4, 834-866, https://doi.org/10.1093/nsr/nwx150,

879   2017a.

880   Li, M., Zhang, Q., Kurokawa, J.-i., Woo, J.-H., He, K., Lu, Z., Ohara, T., Song, Y.,

881   Streets, D. G., Carmichael, G. R., Cheng, Y., Hong, C., Huo, H., Jiang, X., Kang,

882   S., Liu, F., Su, H., and Zheng, B.: MIX: a mosaic Asian anthropogenic emission

883   inventory under the international collaboration framework of the MICS-Asia and

884   HTAP, Atmospheric Chemistry and Physics, 17, 935-963,

885   https://doi.org/10.5194/acp-17-935-2017, 2017b.

886 Li, Q., Zhang, H., Jin, X., Cai, X., and Song, Y.: Mechanism of haze pollution in

887   summer and its difference with winter in the North China Plain, Science of the

888   Total Environment, 806, https://doi.org/10.1016/j.scitotenv.2021.150625, 2022.

889 Li, Q., Wu, B., Liu, J., Zhang, H., Cai, X., and Song, Y.: Characteristics of the

890   atmospheric boundary layer and its relation with $PM_{2.5}$ during haze episodes in

891   winter in the North China Plain, Atmospheric Environment, 223,

892   https://doi.org/10.1016/j.atmosenv.2020.117265, 2020.

893 Li, X.-B., Wang, D.-S., Lu, Q.-C., Peng, Z.-R., and Wang, Z.-Y.: Investigating vertical

894   distribution patterns of lower tropospheric $PM_{2.5}$ using unmanned

895   aerial vehicle measurements, Atmospheric Environment, 173, 62-71,

896   https://doi.org/10.1016/j.atmosenv.2017.11.009, 2018.

897 Liu, C., Huang, J., Wang, Y., Tao, X., Hu, C., Deng, L., Xu, J., Xiao, H.-W., Luo, L.,

898   Xiao, H.-Y., and Xiao, W.: Vertical distribution of $PM_{2.5}$ and

899   interactions with the atmospheric boundary layer during the development stage of

900   a heavy haze pollution event, Science of the Total Environment, 704,

901   https://doi.org/10.1016/j.scitotenv.2019.135329, 2020.

902 Liu, C., Chen, R., Sera, F., Vicedo-Cabrera, A. M., Guo, Y., Tong, S., Coelho, M. S. Z.

903   S., Saldiva, P. H. N., Lavigne, E., Matus, P., Ortega, N. V., Garcia, S. O., Pascal,

904   M., Stafoggia, M., Scortichini, M., Hashizume, M., Honda, Y., Hurtado-Diaz, M.,

905   Cruz, J., Nunes, B., Teixeira, J. P., Kim, H., Tobias, A., Iniguez, C., Forsberg, B.,

906   Astrom, C., Ragettli, M. S., Guo, Y.-L., Chen, B.-Y., Bell, M. L., Wright, C. Y.,

907   Scovronick, N., Garland, R. M., Milojevic, A., Kysely, J., Urban, A., Orru, H.,

908   Indermitte, E., Jaakkola, J. J. K., Ryti, N. R. I., Katsouyanni, K., Analitis, A.,

909   Zanobetti, A., Schwartz, J., Chen, J., Wu, T., Cohen, A., Gasparrini, A., and Kan,

910   H.: Ambient Particulate Air Pollution and Daily Mortality in 652 Cities, New

911   England Journal of Medicine, 381, 705-715,

912   https://doi.org/10.1056/NEJMoa1817364, 2019.

913   Liu, H., Yuan, R., Mei, J., Sun, J., Liu, Q., and Wang, Y.: Scale Properties of Anisotropic
914   and Isotropic Turbulence in the Urban Surface Layer, Boundary-Layer
915   Meteorology, 165, 277-294, https://doi.org/10.1007/s10546-017-0272-z, 2017.

916   Ma, T., Duan, F., He, K., Qin, Y., Tong, D., Geng, G., Liu, X., Li, H., Yang, S., Ye, S.,
917   Xu, B., Zhang, Q., and Ma, Y.: Air pollution characteristics and their relationship
918   with emissions and meteorology in the Yangtze River Delta region during 2014-
919   2016, Journal of Environmental Sciences, 83, 8-20,
920   https://doi.org/10.1016/j.jes.2019.02.031, 2019.

921   McKeen, S., Chung, S. H., Wilczak, J., Grell, G., Djalalova, I., Peckham, S., Gong, W.,
922   Bouchet, V., Moffet, R., Tang, Y., Carmichael, G. R., Mathur, R., and Yu, S.:
923   Evaluation of several PM$_{2.5}$ forecast models using data collected during the
924   ICARTT/NEAQS 2004 field study, Journal of Geophysical Research-Atmospheres,
925   112, https://doi.org/10.1029/2006jd007608, 2007.

926   Miao, Y., Li, J., Miao, S., Che, H., Wang, Y., Zhang, X., Zhu, R., and Liu, S.: Interaction
927   Between Planetary Boundary Layer and PM$_{2.5}$ Pollution in
928   Megacities in China: a Review, Current Pollution Reports, 5, 261-271,
929   https://doi.org/10.1007/s40726-019-00124-5, 2019.

930   Mlawer, E. J., Taubman, S. J., Brown, P. D., Iacono, M. J., and Clough, S. A.: Radiative
931   transfer for inhomogeneous atmospheres: RRTM, a validated correlated-k model
932   for the longwave, Journal of Geophysical Research-Atmospheres, 102, 16663-
933   16682, https://doi.org/10.1029/97jd00237, 1997.

934   Morrison, H., Thompson, G., and Tatarskii, V.: Impact of Cloud Microphysics on the
935   Development of Trailing Stratiform Precipitation in a Simulated Squall Line:
936   Comparison of One- and Two-Moment Schemes, Monthly Weather Review, 137,
937   991-1007, https://doi.org/10.1175/2008mwr2556.1, 2009.

938   Peng, Y., Wang, H., Li, Y., Liu, C., Zhao, T., Zhang, X., Gao, Z., Jiang, T., Che, H., and
939   Zhang, M.: Evaluating the performance of two surface layer schemes for the
940   momentum and heat exchange processes during severe haze pollution in Jing-Jin-
941   Ji in eastern China, Atmospheric Chemistry and Physics, 18, 17421-17435,
942   https://doi.org/10.5194/acp-18-17421-2018, 2018.

943   Pierce, A. M., Loria-Salazar, S. M., Holmes, H. A., and Gustin, M. S.: Investigating

944   horizontal and vertical pollution gradients in the atmosphere associated with an

945   urban location in complex terrain, Reno, Nevada, USA, Atmospheric Environment,

946   196, 103-117, https://doi.org/10.1016/j.atmosenv.2018.09.063, 2019.

947   Qian, Y., Gustafson, W. I., Jr., and Fast, J. D.: An investigation of the sub-grid

948   variability of trace gases and aerosols for global climate modeling, Atmospheric

949   Chemistry and Physics, 10, 6917-6946, https://doi.org/10.5194/acp-10-6917-2010,

950   2010.

951   Quan, J., Dou, Y., Zhao, X., Liu, Q., Sun, Z., Pan, Y., Jia, X., Cheng, Z., Ma, P., Su, J.,

952   Xin, J., and Liu, Y.: Regional atmospheric pollutant transport mechanisms over the

953   North China Plain driven by topography and planetary boundary layer processes,

954   Atmospheric Environment, 221, https://doi.org/10.1016/j.atmosenv.2019.117098,

955   2020.

956   Ren, Y., Zhang, H., Wei, W., Cai, X., and Song, Y.: Determining the fluctuation of $PM_{2.5}$

957   mass concentration and its applicability to Monin-Obukhov similarity, Science of

958   the Total Environment, 710, https://doi.org/10.1016/j.scitotenv.2019.136398, 2020.

959   Ren, Y., Zhang, H., Wei, W., Cai, X., Song, Y., and Kang, L.: A study on atmospheric

960   turbulence structure and intermittency during heavy haze pollution in the Beijing

961   area,   Science   China-Earth   Sciences,   62,   2058-2068,

962   https://doi.org/10.1007/s11430-019-9451-0, 2019a.

963   Ren, Y., Zhang, H., Wei, W., Wu, B., Cai, X., and Song, Y.: Effects of turbulence

964   structure and urbanization on the heavy haze pollution process, Atmospheric

965   Chemistry and Physics, 19, 1041-1057, https://doi.org/10.5194/acp-19-1041-2019,

966   2019b.

967   Ren, Y., Zhang, H., Zhang, X., Li, Q., Cai, X., Song, Y., Kang, L., and Zhu, T.: Temporal

968   and spatial characteristics of turbulent transfer and diffusion coefficient of $PM_{2.5}$,

969   Science   of   the   Total   Environment,   782,

970   https://doi.org/10.1016/j.scitotenv.2021.146804, 2021.

971   Riccobono, F., Schobesberger, S., Scott, C. E., Dommen, J., Ortega, I. K., Rondo, L.,

972   Almeida, J., Amorim, A., Bianchi, F., Breitenlechner, M., David, A., Downard, A.,

973 Dunne, E. M., Duplissy, J., Ehrhart, S., Flagan, R. C., Franchin, A., Hansel, A.,
974 Junninen, H., Kajos, M., Keskinen, H., Kupc, A., Kuerten, A., Kvashin, A. N.,
975 Laaksonen, A., Lehtipalo, K., Makhmutov, V., Mathot, S., Nieminen, T., Onnela,
976 A., Petaja, T., Praplan, A. P., Santos, F. D., Schallhart, S., Seinfeld, J. H., Sipila,
977 M., Spracklen, D. V., Stozhkov, Y., Stratmann, F., Tome, A., Tsagkogeorgas, G.,
978 Vaattovaara, P., Viisanen, Y., Vrtala, A., Wagner, P. E., Weingartner, E., Wex, H.,
979 Wimmer, D., Carslaw, K. S., Curtius, J., Donahue, N. M., Kirkby, J., Kulmala, M.,
980 Worsnop, D. R., and Baltensperger, U.: Oxidation Products of Biogenic Emissions
981 Contribute to Nucleation of Atmospheric Particles, Science, 344, 717-721,
982 https://doi.org/10.1126/science.1243527, 2014.
983 Skamarock, W. C., Klemp, J. B., Dudhia, J., Gill, D. O., and Powers, J. G.: A
984 Description of the Advanced Research WRF Version 3, NCAR Technical Note
985 NCAR/TN-475+STR. June 2008. Mesoscale and Microscale Meteorology
986 Division. National Center for Atmospheric Research. Boulder, 475, 2008.
987 Stull, R. B.: An Introduction to Boundary Layer Meteorology, An Introduction to
988 Boundary Layer Meteorology1988.
989 Sun, T., Che, H., Qi, B., Wang, Y., Dong, Y., Xia, X., Wang, H., Gui, K., Zheng, Y.,
990 Zhao, H., Ma, Q., Du, R., and Zhang, X.: Aerosol optical characteristics and their
991 vertical distributions under enhanced haze pollution events: effect of the regional
992 transport of different aerosol types over eastern China, Atmospheric Chemistry and
993 Physics, 18, 2949-2971, https://doi.org/10.5194/acp-18-2949-2018, 2018.
994 Sun, Y., Song, T., Tang, G., and Wang, Y.: The vertical distribution of
995 $PM_{2.5}$ and boundary-layer structure during summer haze in Beijing,
996 Atmospheric Environment, 74, 413-421,
997 https://doi.org/10.1016/j.atmosenv.2013.03.011, 2013.
998 Tao, H., Xing, J., Zhou, H., Pleim, J., Ran, L., Chang, X., Wang, S., Chen, F., Zheng,
999 H., and Li, J.: Impacts of improved modeling resolution on the simulation of
1000 meteorology, air quality, and human exposure to $PM_{2.5}$, O_3 in Beijing, China,
1001 Journal of Cleaner Production, 243, https://doi.org/10.1016/j.jclepro.2019.118574,
1002 2020.

1003 Tuccella, P., Curci, G., Visconti, G., Bessagnet, B., Menut, L., and Park, R. J.: Modeling
1004   of gas and aerosol with WRF-Chem over Europe: Evaluation and sensitivity study,
1005   Journal of Geophysical Research-Atmospheres, 117,
1006   https://doi.org/10.1029/2011jd016302, 2012.

1007 Von Kuhlmann, R., Lawrence, M. G., Crutzen, P. J., and Rasch, P. J.: A model for
1008   studies of tropospheric ozone and nonmethane hydrocarbons: Model description
1009   and ozone results, Journal of Geophysical Research-Atmospheres, 108,
1010   https://doi.org/10.1029/2002jd002893, 2003.

1011 Wang, H., Peng, Y., Zhang, X., Liu, H., Zhang, M., Che, H., Cheng, Y., and Zheng, Y.:
1012   Contributions to the explosive growth of $PM_{2.5}$ mass due to aerosol-radiation
1013   feedback and decrease in turbulent diffusion during a red alert heavy haze in
1014   Beijing-Tianjin-Hebei, China, Atmospheric Chemistry and Physics, 18, 17717-
1015   17733, https://doi.org/10.5194/acp-18-17717-2018, 2018.

1016 Wei, W., Zhang, H., Cai, X., Song, Y., Bian, Y., Xiao, K., and Zhang, H.: Influence of
1017   Intermittent Turbulence on Air Pollution and Its Dispersion in Winter 2016/2017
1018   over Beijing, China, Journal of Meteorological Research, 34, 176-188,
1019   https://doi.org/10.1007/s13351-020-9128-4, 2020.

1020 Wei, W., Zhang, H., Wu, B., Huang, Y., Cai, X., Song, Y., and Li, J.: Intermittent
1021   turbulence contributes to vertical dispersion of $PM_{2.5}$ in the North China Plain:
1022   cases from Tianjin, Atmospheric Chemistry and Physics, 18, 12953-12967,
1023   https://doi.org/10.5194/acp-18-12953-2018, 2018.

1024 Wiedinmyer, C., Akagi, S. K., Yokelson, R. J., Emmons, L. K., Al-Saadi, J. A., Orlando,
1025   J. J., and Soja, A. J.: The Fire INventory from NCAR (FINN): a high resolution
1026   global model to estimate the emissions from open burning, Geoscientific Model
1027   Development, 4, 625-641, https://doi.org/10.5194/gmd-4-625-2011, 2011.

1028 Wild, O., Zhu, X., and Prather, M. J.: Fast-j: Accurate simulation of in- and below-
1029   cloud photolysis in tropospheric chemical models, Journal of Atmospheric
1030   Chemistry, 37, 245-282, https://doi.org/10.1023/a:1006415919030, 2000.

1031 WRAP – Western Regional Air Partnership: 2002 Fire Emission Inventory for the
1032   WRAP   Region   –   Phase   II,   Project   No.178-6,   available   at:

1033   http://www.wrapair.org/forums/fejf/tasks/FEJFtask7PhaseII.html (last access: 30
1034   September 2021), 2005.

1035   Wu, H., Li, Z., Li, H., Luo, K., Wang, Y., Yan, P., Hu, F., Zhang, F., Sun, Y., Shang, D.,
1036   Liang, C., Zhang, D., Wei, J., Wu, T., Jin, X., Fan, X., Cribb, M., Fischer, M. L.,
1037   Kulmala, M., and Petaja, T.: The impact of the atmospheric turbulence-
1038   development tendency on new particle formation: a common finding on three
1039   continents, National Science Review, 8, https://doi.org/10.1093/nsr/nwaa157,
1040   2021.

1041   Xu, J., Yan, F., Xie, Y., Wang, F., Wu, J., and Fu, Q.: Impact of meteorological
1042   conditions on a nine-day particulate matter pollution event observed in December
1043   2013,   Shanghai,   China,   Particuology,   20,   69-79,
1044   https://doi.org/10.1016/j.partic.2014.09.001, 2015.

1045   Ye, X., Song, Y., Cai, X., and Zhang, H.: Study on the synoptic flow patterns and
1046   boundary layer process of the severe haze events over the North China Plain in
1047   January   2013,   Atmospheric   Environment,   124,   129-145,
1048   https://doi.org/10.1016/j.atmosenv.2015.06.011, 2016.

1049   Yin, P., Brauer, M., Cohen, A., Burnett, R. T., Liu, J., Liu, Y., Liang, R., Wang, W., Qi,
1050   J., Wang, L., and Zhou, M.: Long-term Fine Particulate Matter Exposure and
1051   Nonaccidental and Cause-specific Mortality in a Large National Cohort of Chinese
1052   Men, Environmental Health Perspectives, 125, https://doi.org/10.1289/ehp1673,
1053   2017.

1054   Yuan, R., Luo, T., Sun, J., Liu, H., Fu, Y., and Wang, Z.: A new method for estimating
1055   aerosol mass flux in the urban surface layer using LAS technology, Atmospheric
1056   Measurement Techniques, 9, 1925-1937, https://doi.org/10.5194/amt-9-1925-2016,
1057   2016.

1058   Zaveri, R. A. and Peters, L. K.: A new lumped structure photochemical mechanism for
1059   large-scale applications, Journal of Geophysical Research-Atmospheres, 104,
1060   30387-30415, https://doi.org/10.1029/1999jd900876, 1999.

1061   Zaveri, R. A., Easter, R. C., Fast, J. D., and Peters, L. K.: Model for Simulating Aerosol
1062   Interactions and Chemistry (MOSAIC), Journal of Geophysical Research-

1063 Atmospheres, 113, https://doi.org/10.1029/2007jd008782, 2008.

1064 Zhang, H., Zhang, X., Li, Q., Cai, X., Fan, S., Song, Y., Hu, F., Che, H., Quan, J., Kang,
1065   L., and Zhu, T.: Research progress on estimation of atmospheric boundary layer
1066   height, Acta Meteorologica Sinica, 78, 522-536, 2020.

1067 Zhang, L., Zhang, H., Li, Q., Cai, X., and Song, Y.: Vertical dispersion mechanism of
1068   long-range transported dust in Beijing: Effects of atmospheric turbulence,
1069   Atmospheric Research, 269, https://doi.org/10.1016/j.atmosres.2022.106033,
1070   2022.

1071 Zhang, L., Sun, J. Y., Shen, X. J., Zhang, Y. M., Che, H., Ma, Q. L., Zhang, Y. W.,
1072   Zhang, X. Y., and Ogren, J. A.: Observations of relative humidity effects on aerosol
1073   light scattering in the Yangtze River Delta of China, Atmospheric Chemistry and
1074   Physics, 15, 8439-8454, https://doi.org/10.5194/acp-15-8439-2015, 2015a.

1075 Zhang, M., Zhao, C., Yang, Y., Du, Q., Shen, Y., Lin, S., Gu, D., Su, W., and Liu, C.:
1076   Modeling sensitivities of BVOCs to different versions of MEGAN emission
1077   schemes in WRF-Chem (v3.6) and its impacts over eastern China, Geoscientific
1078   Model Development, 14, 6155-6175, https://doi.org/10.5194/gmd-14-6155-2021,
1079   2021.

1080 Zhang, R., Wang, G., Guo, S., Zarnora, M. L., Ying, Q., Lin, Y., Wang, W., Hu, M., and
1081   Wang, Y.: Formation of Urban Fine Particulate Matter, Chemical Reviews, 115,
1082   3803-3855, https://doi.org/10.1021/acs.chemrev.5b00067, 2015b.

1083 Zhang, Z., Xu, X., Qiao, L., Gong, D., Kim, S.-J., Wang, Y., and Mao, R.: Numerical
1084   simulations of the effects of regional topography on haze pollution in Beijing,
1085   Scientific Reports, 8, https://doi.org/10.1038/s41598-018-23880-8, 2018.

1086 Zhao, C., Liu, X., Leung, L. R., and Hagos, S.: Radiative impact of mineral dust on
1087   monsoon precipitation variability over West Africa, Atmospheric Chemistry and
1088   Physics, 11, 1879-1893, https://doi.org/10.5194/acp-11-1879-2011, 2011.

1089 Zhao, C., Leung, L. R., Easter, R., Hand, J., and Avise, J.: Characterization of speciated
1090   aerosol direct radiative forcing over California, Journal of Geophysical Research-
1091   Atmospheres, 118, 2372-2388, https://doi.org/10.1029/2012jd018364, 2013a.

1092 Zhao, C., Li, Y., Zhang, F., Sun, Y., and Wang, P.: Growth rates of fine aerosol particles

1093   at a site near Beijing in June 2013, Advances in Atmospheric Sciences, 35, 209-

1094   217, https://doi.org/10.1007/s00376-017-7069-3, 2018.

1095 Zhao, C., Chen, S., Leung, L. R., Qian, Y., Kok, J. F., Zaveri, R. A., and Huang, J.:

1096   Uncertainty in modeling dust mass balance and radiative forcing from size

1097   parameterization, Atmospheric Chemistry and Physics, 13, 10733-10753,

1098   https://doi.org/10.5194/acp-13-10733-2013, 2013b.

1099 Zhao, C., Hu, Z., Qian, Y., Leung, L. R., Huang, J., Huang, M., Jin, J., Flanner, M. G.,

1100   Zhang, R., Wang, H., Yan, H., Lu, Z., and Streets, D. G.: Simulating black carbon

1101   and dust and their radiative forcing in seasonal snow: a case study over North

1102   China with field campaign measurements, Atmospheric Chemistry and Physics, 14,

1103   11475-11491, https://doi.org/10.5194/acp-14-11475-2014, 2014.

1104 Zhao, C., Huang, M., Fast, J. D., Berg, L. K., Qian, Y., Guenther, A., Gu, D.,

1105   Shrivastava, M., Liu, Y., Walters, S., Pfister, G., Jin, J., Shilling, J. E., and Warneke,

1106   C.: Sensitivity of biogenic volatile organic compounds to land surface

1107   parameterizations and vegetation distributions in California, Geoscientific Model

1108   Development, 9, 1959-1976, https://doi.org/10.5194/gmd-9-1959-2016, 2016.

1109 Zhao, X. J., Zhao, P. S., Xu, J., Meng, W., Pu, W. W., Dong, F., He, D., and Shi, Q. F.:

1110   Analysis of a winter regional haze event and its formation mechanism in the North

1111   China Plain, Atmospheric Chemistry and Physics, 13, 5685-5696,

1112   https://doi.org/10.5194/acp-13-5685-2013, 2013c.

1113 Zhong, J., Zhang, X., Dong, Y., Wang, Y., Liu, C., Wang, J., Zhang, Y., and Che, H.:

1114   Feedback effects of boundary-layer meteorological factors on cumulative

1115   explosive growth of $PM_{2.5}$ during winter heavy pollution episodes in Beijing from

1116   2013 to 2016, Atmospheric Chemistry and Physics, 18, 247-258,

1117   https://doi.org/10.5194/acp-18-247-2018, 2018.

1118

1119

1120

1121

1122

1123

1124

1125   **Table 1** WRF-Chem model configuration

Horizontal resolution	25 km & 5 km & 1 km
Domain size	140 x 105 & 250 x 250 & 150 x 150
Simulation period	5 March to 21 March 2019
Gas-phase chemistry scheme	SAPRC99 mechanism
Radiation scheme	Fast-J
PBL scheme	YSU scheme
Microphysics scheme	Morrison two-moment scheme
Land surface scheme	Noah land-surface scheme
Cumulus scheme	Kain-Fritsch (25 km grid only)
Surface layer scheme	Revised MM5 Monin-Obukhov scheme
Longwave radiation scheme	RRTMG scheme
Shortwave radiation scheme	RRTMG scheme

1126
1127
1128
1129
1130
1131
1132
1133
1134
1135
1136
1137
1138
1139
1140
1141
1142
1143
1144
1145
1146
1147
1148
1149
1150
1151
1152
1153
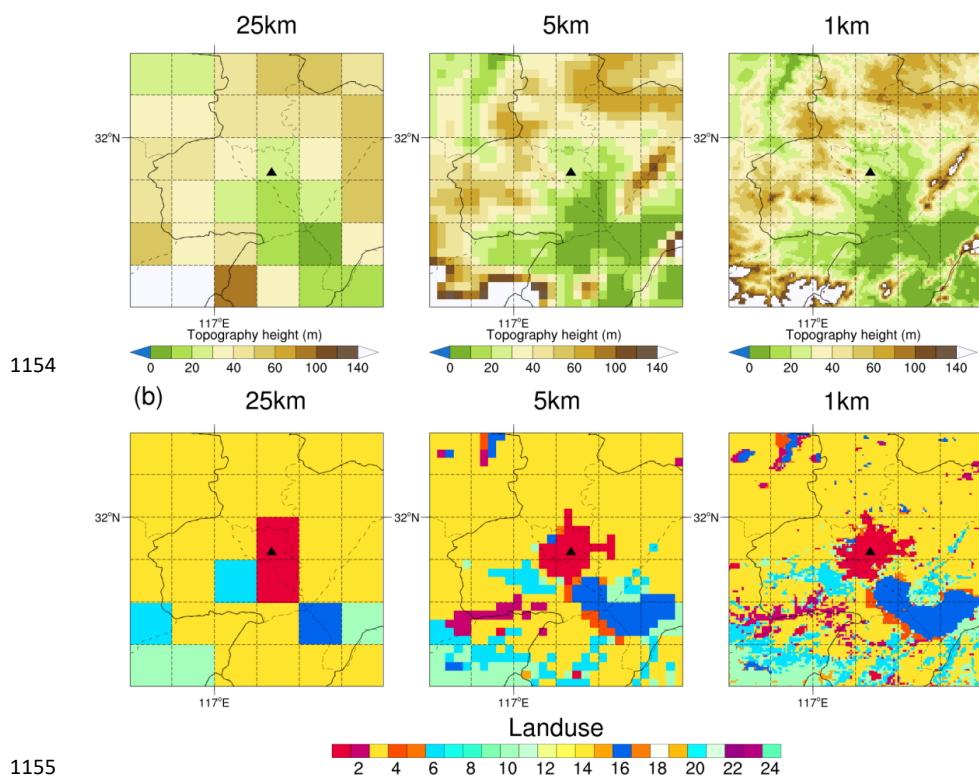
Figure 1. (a) The terrain height (m) in the study area for 25-km (left), 5-km (middle), and 1-km (right) resolution simulations, respectively; (b) Spatial distribution of land use types in the study area for 25-km (left), 5-km (middle), and 1-km (right) resolution simulations, respectively. The solid black triangle indicates the location of the USTC site.
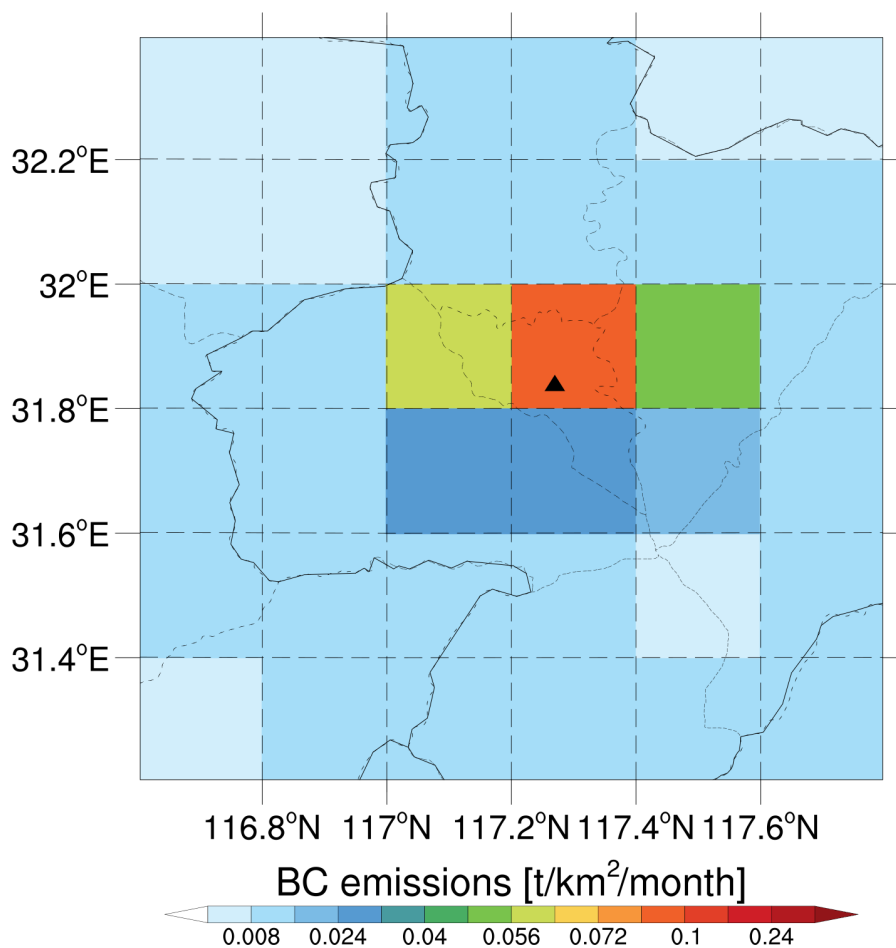
Figure 2. Spatial distribution of BC emissions in the study area. The solid black

triangle indicates the location of the USTC site.
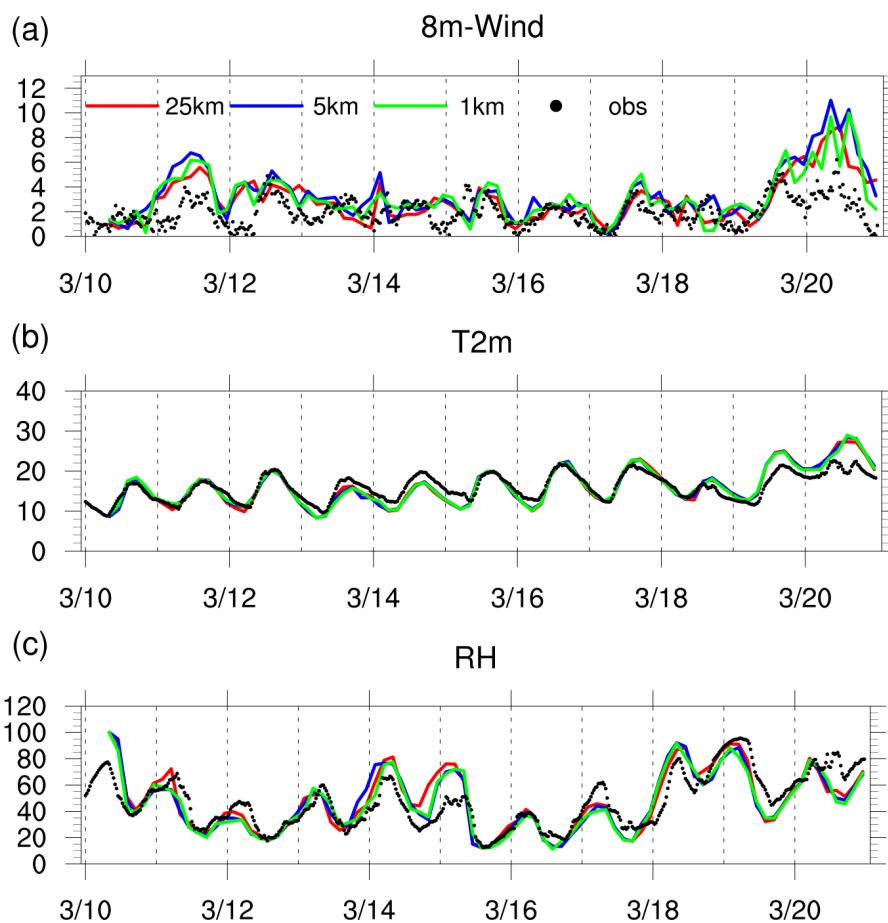
Figure 3. Time series at USTC meteorological tower observation site of observed

(black dot) and simulated wind speed at 8 m (top, unit: m s⁻¹), temperature at 2 m

(middle, unit: °C), and relative humidity (bottom, unit: %) for 25-km (solid red line)

resolution, 5-km (solid blue line) resolution, and 1-km (solid green line) resolution,
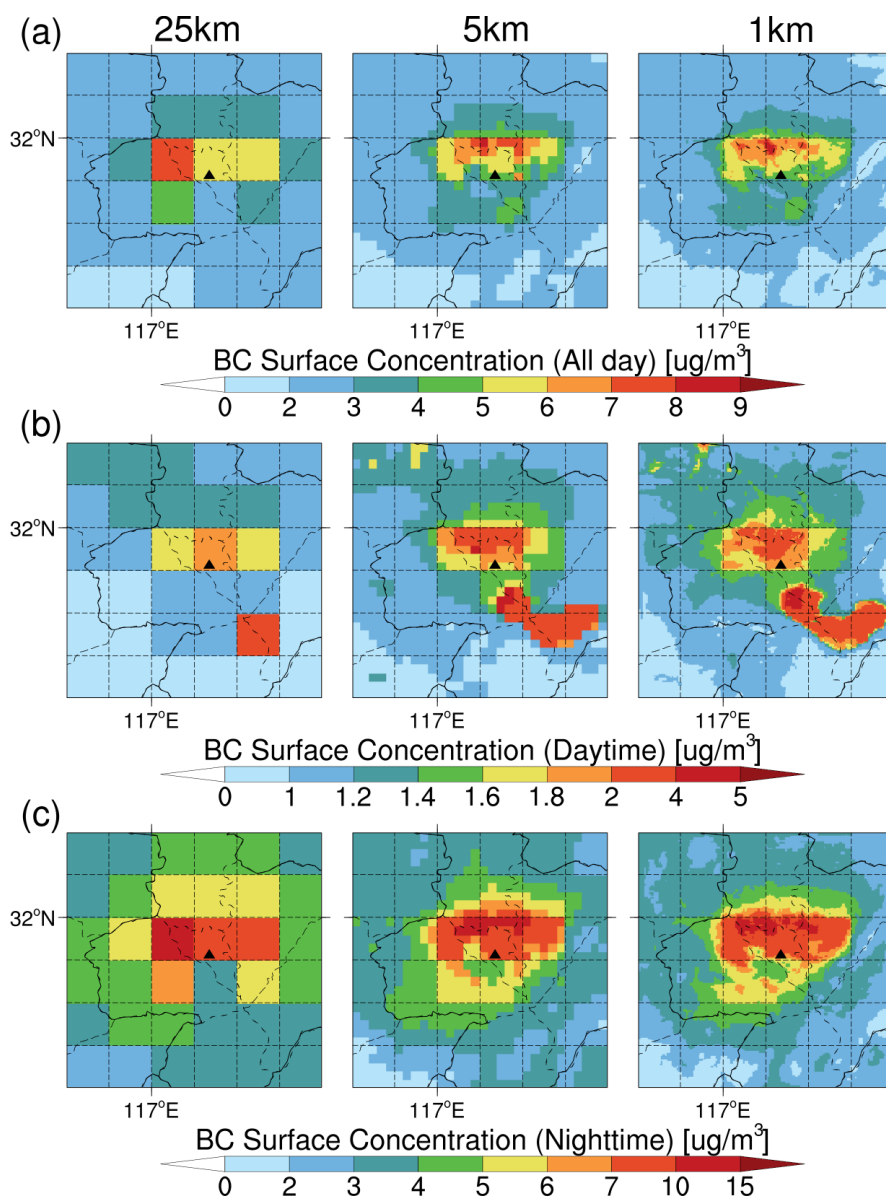
respectively.

Figure 4. Spatial distribution of the BC surface concentration in the study area for 25-km (left), 5-km (middle), and 1-km (right) resolution simulations of the whole day (top), the daytime (middle), and the nighttime (bottom), respectively. The solid black triangle indicates the location of the USTC site.

1202
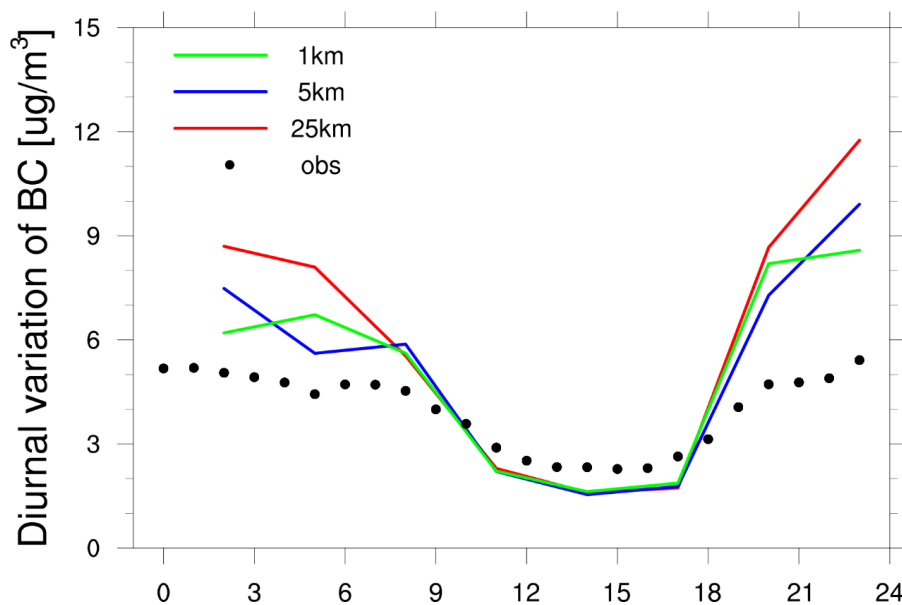
Figure 5. Diurnal variation of BC surface concentrations within 24 h averaged over

the Hefei region (within the range of Figure 1a) during the study period for 25-km

(solid red line), 5-km (solid blue line), and 1-km (solid green line) resolution

simulations and observations (black dot). Both the simulated results and observations

are sampled at the model output frequency, i.e., 3-hourly.

1203

1204

1205

1206

1207

1208

1209

1210

1211

1212

1213

1214

1215

1216

1217

1218

1219

1220
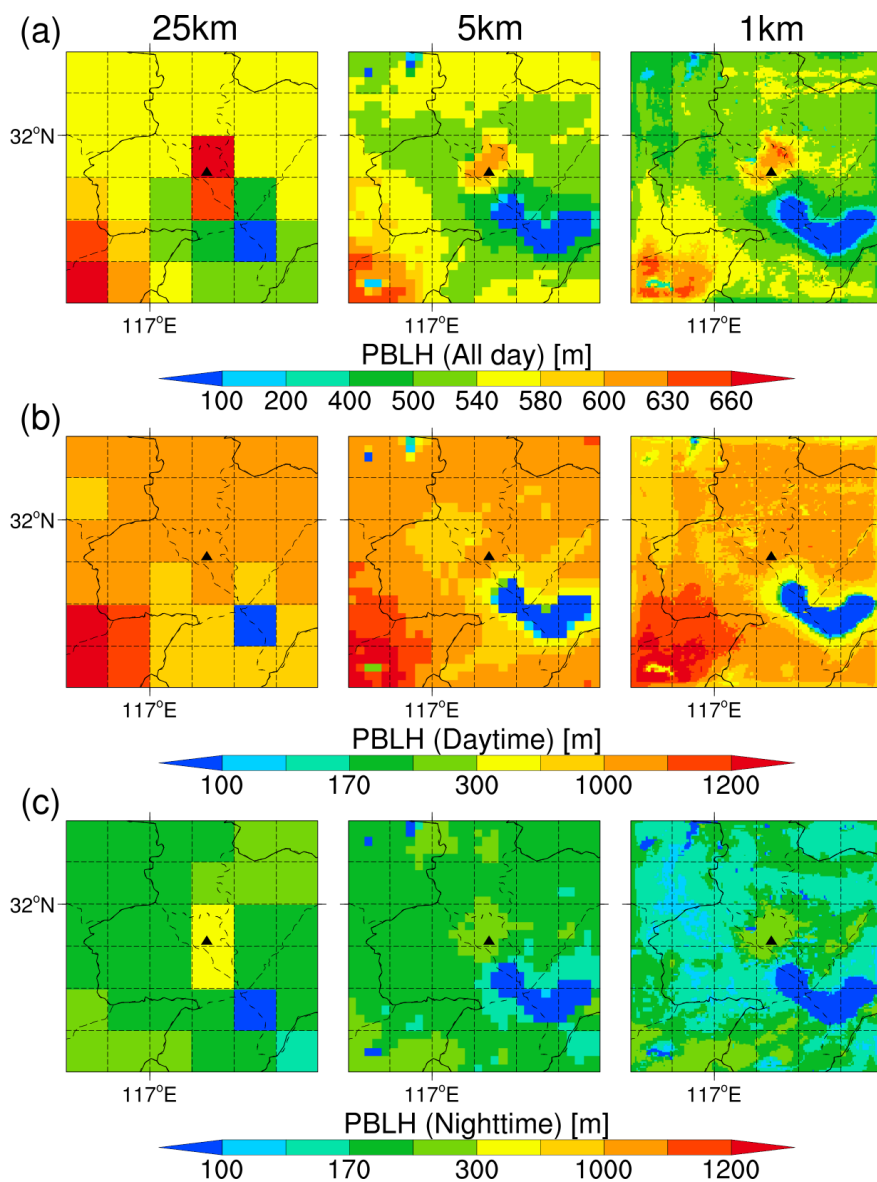
Figure 6. Spatial distribution of the PBL height in the study area for 25-km (left), 5-km (middle), and 1-km (right) resolution simulations of the whole day (top), the daytime (middle), and the nighttime (bottom), respectively. The solid black triangle indicates the location of the USTC site.
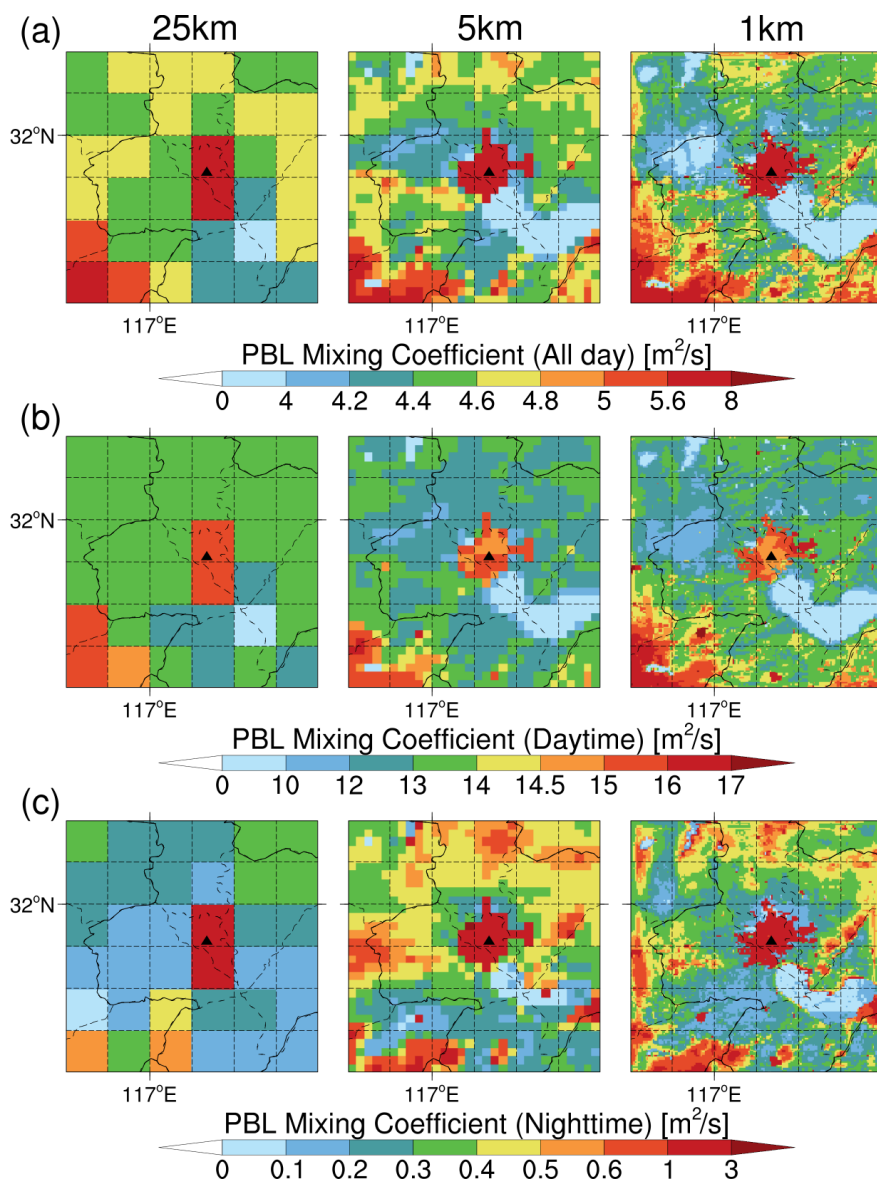
Figure 7. Spatial distribution of PBL mixing coefficients in the study area for 25-km (left), 5-km (middle), and 1-km (right) resolution simulations of the whole day (top), the daytime (middle), and the nighttime (bottom), respectively. The solid black triangle indicates the location of the USTC site.
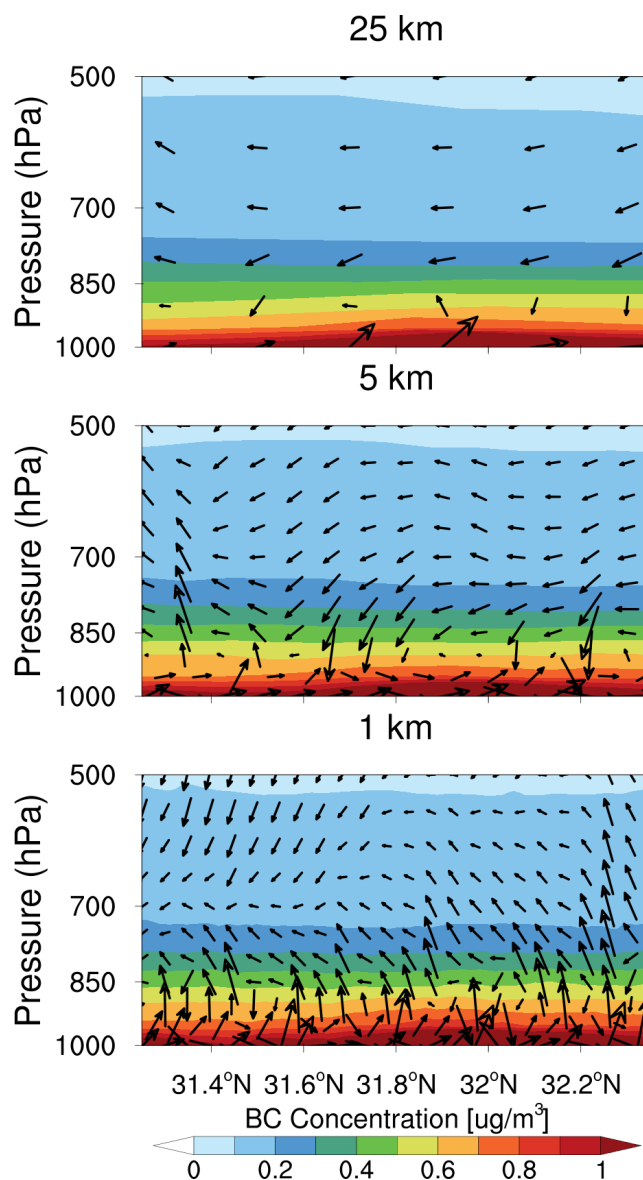
Figure 8. The latitude-pressure cross section of BC concentrations and wind speed

flux along the USTC site for 25-km (top), 5-km (middle), and 1-km (bottom)

resolution simulations of the whole day, respectively. Vector arrows are the

combination of wind speed fluxes v and w, with the vertical wind speed flux being

multiplied by 100 for visibility. The shaded contours represent BC concentrations at

each pressure level.
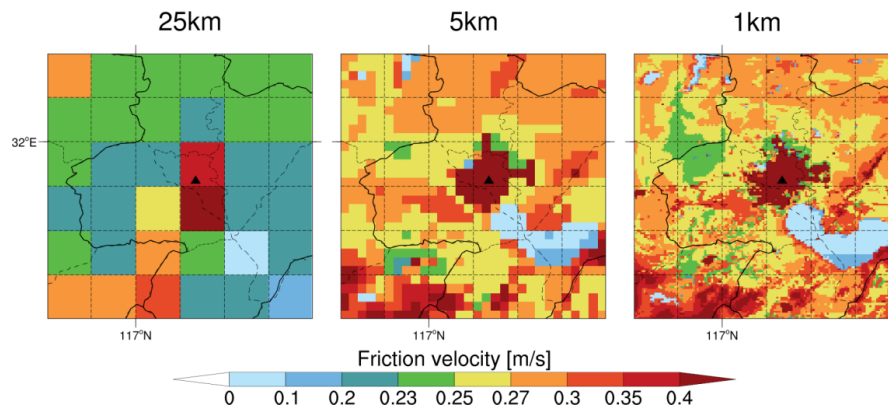
Figure 9. Spatial distribution of friction velocity in the study area for 25-km (left), 5-km (middle), and 1-km (right) resolution simulations of the whole day, respectively. The solid black triangle indicates the location of the USTC site.
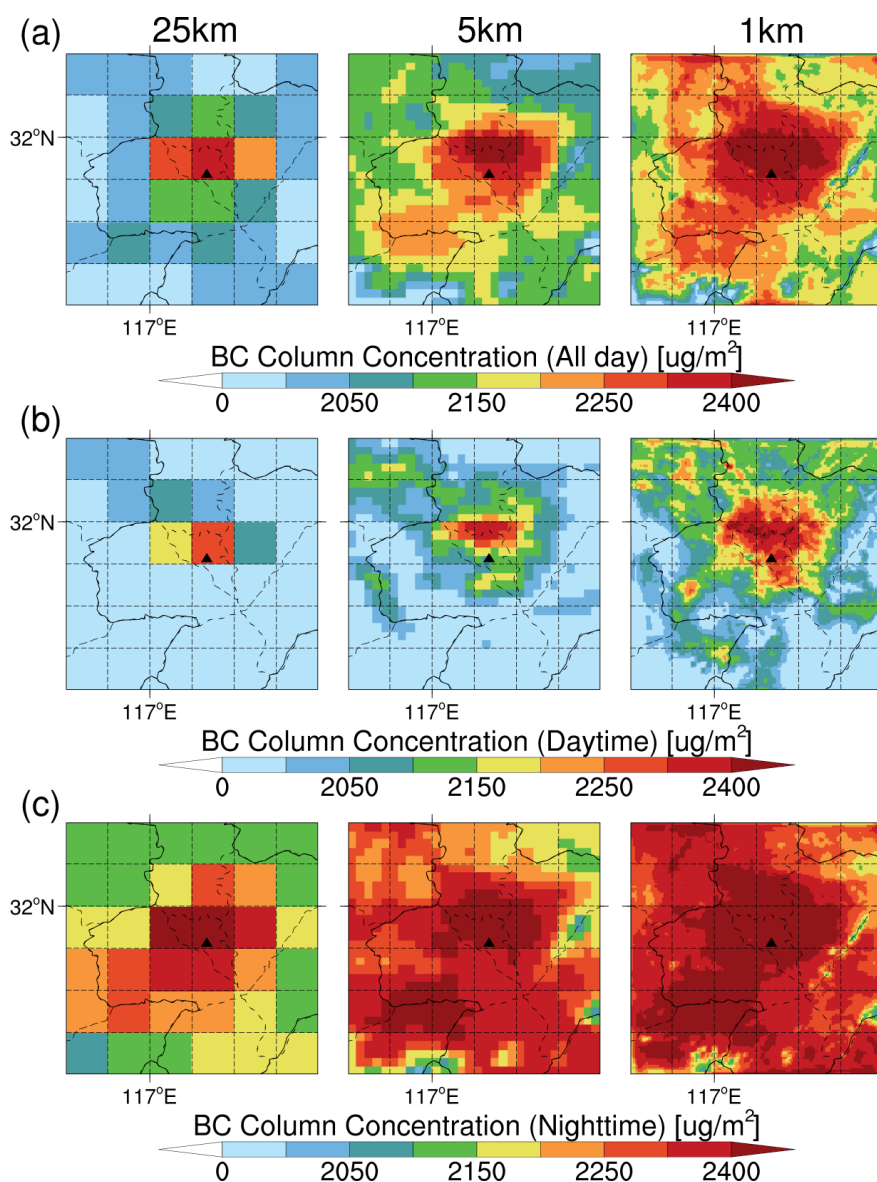
Figure 10. Spatial distribution of the BC column concentration in the study area for 25-km (left), 5-km (middle), and 1-km (right) resolution simulations of the whole day (top), the daytime (middle), and the nighttime (bottom), respectively. The solid black triangle indicates the location of the USTC site.
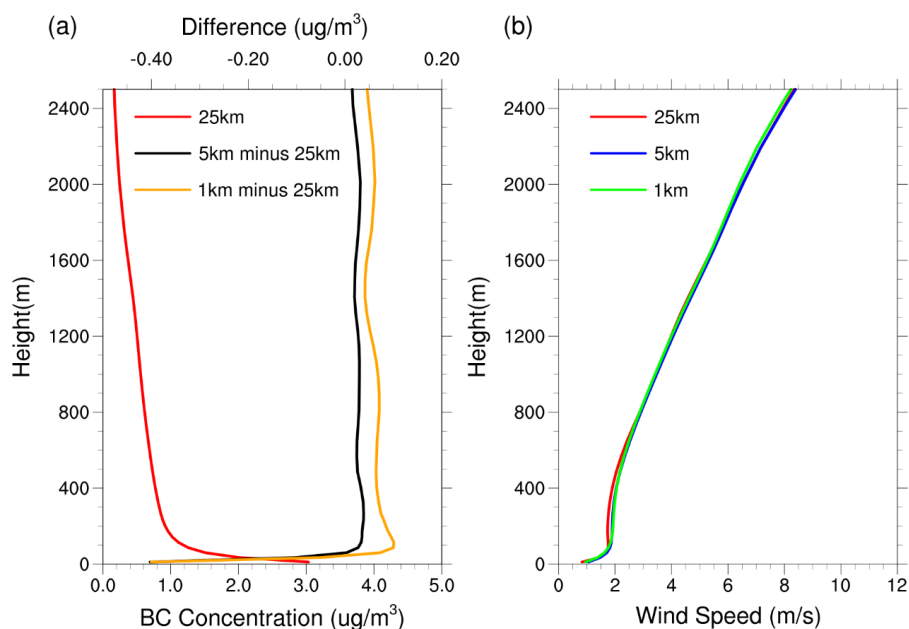
Figure 11. (a) Vertical profiles of BC concentrations simulated at 25-km resolution

(solid red line), the difference between 5-km and 25-km resolutions (solid black line),

and the difference between 1-km and 25-km resolutions (solid orange line) averaged

over the study area for the whole day, respectively. (b) Vertical profiles of wind speed

simulated at 25-km resolution (solid red line), 5-km resolution (solid blue line), and 1-

km resolution (solid green line) averaged over the study area for the whole day,
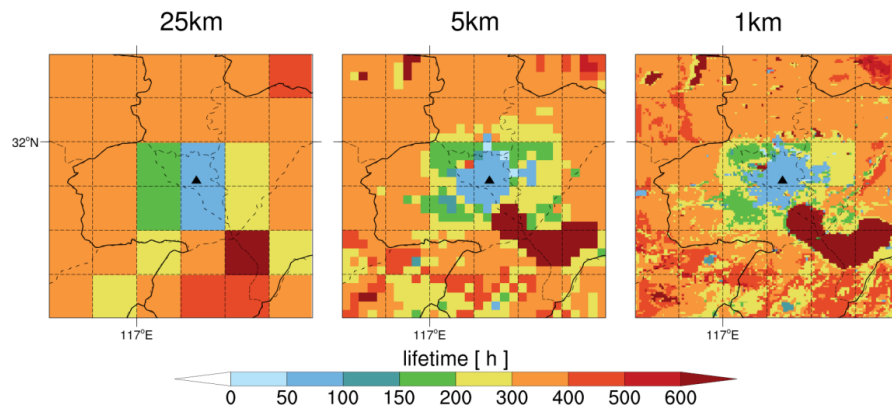
respectively.

Figure 12. Spatial distribution of the lifetime in the study area for 25-km (left), 5-km
(middle), and 1-km (right) resolution simulations of the whole day, respectively. The
solid black triangle indicates the location of the USTC site.